Exotic wakes of flapping fins

Schnipper, Teis; Andersen, Anders Peter; Bohr, Tomas; Sørensen, Jens Nørkær; Aref, Hassan

Publication date:
2011

Document Version
Publisher's PDF, also known as Version of record

Exotic wakes of flapping fins

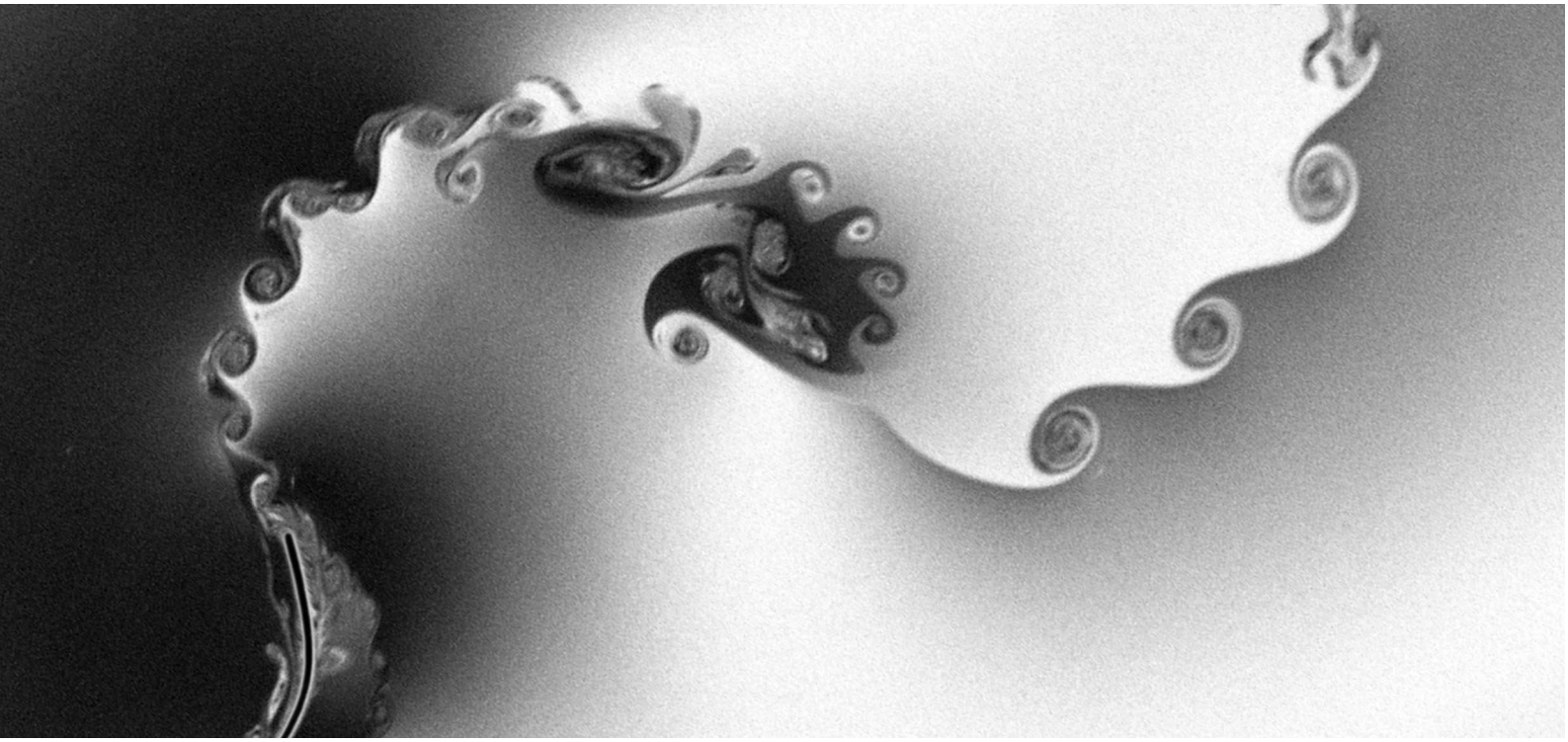

Ph.d. dissertation

Teis Schnipper

February 9, 2012

DTU Physics
Department of Physics

Fluid·DTU
Center for Fluid Dynamics at DTU

Exotic wakes of flapping fins

Teis Schnipper

Ph.d. dissertation

Supervisors	Anders Andersen	Department of Physics, DTU
	Hassan Aref	DTU and Virginia Tech, USA
	Tomas Bohr	Department of Physics, DTU
	Jens Nørkjær Sørensen	Department of Mechanical Engineering, DTU

Department of Physics and Center for Fluid Dynamics
Technical University of Denmark
2800 Kgs. Lyngby
Denmark

February 9, 2012

Preface

This dissertation is submitted as a partial fulfillment of the requirements to obtain the degree of philosophiae doctor at the Technical University of Denmark (DTU).

The major part of scientific work was carried out at the Department of Physics, DTU, in the period August 2007 to August 2010. The work presented in chapter 7 was carried out during an internship (November 2009 to February 2010) in the Applied Mathematics Laboratory, Courant Institute of Mathematical Sciences, New York University.

The ph.d. was funded, in equal parts, by a Niels Bohr visiting professorship from the Danish National Research Foundation (Danmarks Grundforskningsfond) and by the Department of Physics, DTU. Both are greatly acknowledged for the financial support.

Teis Schnipper
November 2010

Summary

We present, in 8 chapters, experiments on and numerical simulations of bodies flapping in a fluid. Focus is predominantly on a rigid foil, a model fish, that performs prescribed pitching oscillations where the foil rotates around its leading edge.

In a flowing soap film is measured, with unprecedented accuracy, the vortex wake structure behind the flapping foil in the space spanned by dimensionless flapping frequency $0 < \mathrm{St}_D < 0.3$ and amplitude $0 < A_D < 2$. We measure not only the ubiquitous von Kármán wake, but also wakes where up to sixteen vortices are shed each oscillation period. The wake measurements are supplemented with numerical simulations of the flow and fluid forces, in settings relevant for the experiments. It is shown that wake transitions and average fluid forces are described by a single parameter, the Strouhal number, which is a measure of both the dimensionless foil tip-speed and the strength ratio of the vortices formed at the foil's leading and trailing edge. The simulated vortex particles and measured thickness variations in the soap film show similar behaviour which indicates that the soap film provides a good approximation the flow of a two-dimensional incompressible and Newtonian fluid. Also, measurements of the swimming speed of a pitching foil in a water tank are presented.

Finally, an experimental study of the surprisingly strong fluid-mediated interaction of two tandem flappers is presented. It is shown that a passively flapping flag in general is affected by its downstream neighbour. When this neighbour is a second flag close by, they synchronise in frequency and the leader experiences a reduced drag compared to that on the lone flag. In case the follower is replaced by a flapping plate, upstream synchronisation and drag reduction is again found over a wide range of frequencies. Drag reductions up to a factor 3 are measured.

Many results presented are obtained through flow visualisations. A great effort is made to produce visualisations of primarily high scientific quality, but often also with a certain aesthetic appeal.

Dansk resumé

Hvordan ser kølvandet af en svømmende fisk ud, og kan vi forstå kræfterne på fisken ved at betragte dens 'fodspor' i vandet? I denne afhandling præsenteres en række eksperimenter og numeriske beregninger, der undersøger hvirveldannelse ved, kølvandsstruktur bag og kræfter på baskende finner, dvs. stiliserede 'fisk'. Megen indsigt opnås igennem visualisering af strømningerne. Der er generelt lagt vægt på visualiseringer af primært høj videnskabelig kvalitet, men ofte også med et æstetisk udtryk.

I en sæbehinde der strømmer lodret nedefter måles i høj detaljeringsgrad de periodiske hvirvelkølvand bag en oscillerende finne. Ved at variere frekvens og amplitude findes en stor botanik af periodiske kølvandsstrukturer. Således måles både den klassiske 'von Kármán hvirvel allé', hvor 2 modsat roterende hvirvler dannes per oscillationsperiode, men også komplicerede og hidtil ukendte kølvand hvori op til 16 hvirvler dannes per periode. Kølvandstyperne præsenteres i et 'landkort' der udspændes af oscillationsfrekvens og -amplitude. Simple matematiske modeller, der beskriver placeringen af kølvandsstrukturer i landkortet, præsenteres. Kølvandsmålingerne suppleres med numeriske beregninger af strømningen ved og kræfterne på finnen. Simuleringerne leder også til udvikling af en matematisk model for kræfterne. Resultaterne diskuteres i forhold til målinger af svømmefarten af en oscillerende finne i et vandkar. Sidstnævnte viser, at svømmefarten af en baskende finne er proportional med oscillationsfrekvensen.

Endelig præsenteres et eksperimentelt studie af to oscillerende legemer i tandem, der vekselvirker i overraskende grad via strømningerne. Et passivt blafrende flag mærker generelt tilstedeværelsen af sin nedstrøms nabo. Når denne er et identisk flag, synkroniserer de to i frekvens mens det forreste flag oplever en reduceret strømningsmodstand. Erstattes det bagerste flag med en oscillerende plade opnås også synkronisering, over et stort frekvensområde, af det opstrøms flag hvis strømningsmodstand kan reduceres med en faktor 3.

List of included papers

The dissertation is based on three publications and one submitted manuscript that are included in the appendix. Furthermore, one manuscript (not included) is currently being prepared for submission. The main results have been presented at three international conferences and one national conference.

Article I
Teis Schnipper, Anders Andersen and Tomas Bohr
Vortex wakes of a flapping foil
Journal of Fluid Mechanics **633**, 411–423 (2009).

Article II
Anders Andersen, Tomas Bohr and Teis Schnipper
Separation vortices and pattern formation
Theoretical and Computational Fluid Dynamics **24**, 329–334 (2010).

Article III
Teis Schnipper, Laust Tophøj, Anders Andersen and Tomas Bohr
Japanese fan flow
Physics of Fluids **22**, 091102 (2010).

Manuscript I
Teis Schnipper and Jun Zhang
Upstream Drafting of a Flexible Body by its Downstream Neighbor
Submitted (2010).

Manuscript II
Anders Andersen, Tomas Bohr, Teis Schnipper and Jens H. Walther
Fluid Forces and vortex wakes of a flapping foil
In preparation.

Acknowledgements

During my time as a ph.d. student, I have worked with, learned from and laughed with many good people. In particular, I am grateful to the following.

Supervisors Anders Andersen, Hassan Aref, Tomas Bohr and Jens N. Sørensen. For inspiration, collaboration, discussions and endless help, and also for gentle pushes in the back when needed. Erik Hansen at the mechanical workshop—your interest in physics and excellent craftsmanship are invaluable. Jens H. Walther at the Department of Mechanical Engineering for flow and force simulations of the pitching foil and good collaboration. Ph.d. students Johan Rønby and Laust Tophøj for your friendship, sharp brains and many good discussions that include subjects not limited to scientific realms. In particular a big thanks to Laust for help with proof-reading. And not to forget Dorte Glass, the department secretary, for always being cheerful and helpful to an extend I find hard to comprehend.

During 4 months from November 2009 I was an intern at the Applied Mathematics Laboratory, Courant Institute of Mathematical Sciences, New York University. I was warmly welcomed by Jun Zhang and I often think back to the days in AML lab with a smile. For the inspirational work, for letting me work in your laboratory, and for the many good laughs: Thank you Jun! Also I would like to thank Mike, Stephen, Annie, Bin, Christel, Enkeleida, Eric, Shawn, Tamar and Trush and for many good discussions and company.

My family for support and sincere interest in my doing the past three years. Last, but still first and foremost, the warmest thoughts to Nina. For your incredible and invaluable support and patience, and for reminding me that there are more important things in life than physics.

Contents

Chapter 1

Introduction

Karl Hiemenz worked hard in the early 20th century to optimise an experimental set-up for the study of flow past circular cylinders. Together with his supervisor Ludwig Prandtl he wanted to understand the position where flow streamlines separate close to the cylinder. Despite careful construction of the set-up, the expected symmetrical flow field did not appear. Instead regions of swirling fluid with an alternating sense of rotation formed—one after the other—and were succesively shed into the wake of the cylinder. Prandtl believed that the vortex shedding was due to imperfections of the set-up and encouraged Hiemenz to adjust and machine the set-up to beyond perfection. Little did they know that the periodic detachment of vortices was, in fact, an intrinsic phenomenon of the cylinder flow (von Kármán, 1957).

What Hiemenz and Prandtl observed, the periodic vortex wake, is today known as the *von Kármán wake*. The name is after Theodore von Kármán who at the same time was working in Prandtl's laboratory in Göttingen and analysed the stability of the vortex configuration in the wake. It is only fair to mention the French professor Henri Bénard, who already in the late 19th century studied the periodicity of the vortex wake (Wesfreid, 2006). Bénard was disappointed that the phenomenon was named after von Kármán, and the latter proposed that "*. . . what in Berlin and London is called 'Kármán Street' in Paris shall be called 'Avenue de Henri Bénard.'*" This proposition settled, in the opinion by von Kármán at least, the dispute. The wake is occasionally today referred diplomatically to as the 'Bénard-von Kármán wake'. Here we will, for brevity, call it the 'von Kármán wake'.

Experiments on periodic vortex wakes are central in this dissertation. This chapter gives a general introduction to peroidic vortex wakes behind bluff bodies, of which the flow past a cylinder is a classical example that is still attracting a great deal of attention from researchers. The flow is generally complicated, and this chapter will

focus on cases where the flow is predominantly two-dimensional and the cylinder does not move in response to the flow. For more details see the thorough review papers on the cylinder wake (Williamson, 1996) and vortex-induced vibrations (Williamson & Govardhan, 2004). Then, the active modulation of wakes through prescribed oscillation of a rigid body, like a cylinder or a flapping foil, is introduced. In chapters 3–7 we will study situations in which a foil or a filament oscillates in a flow. We will focus on the following questions: Which *wake types* can a flapping foil create? What are the *fluid forces* that the foil experiences? Can two flappers interact via *fluid-mediated forces*? We will adress these questions with experiments and simulations at moderate Reynolds number, $\mathrm{Re} \sim 300$.

1.1 Flow past a cylinder

A bluff body subjected to a flow will experience fluid forces and in turn alter the flow. The perhaps most studied such system is a cylinder in a uniform free streaming flow. The flow is characterised by the Reynolds number

$$\mathrm{Re} \equiv \frac{DU}{\nu}, \tag{1.1}$$

where D is the cylinder diameter, U is the free streaming flow speed and ν is the kinematic viscosity of the fluid.

Depending on the Reynolds number, qualitatively different flows are observed cf. figure 1.1. When the Reynolds number is small, i.e. $\mathrm{Re} \ll 1$, viscosity dominates inertial effects. Here, the fluid 'slowly' crawls past the cylinder, like one can imagine thick honey crawling past a spoon. In this low Reynolds number limit the flow is called creeping flow. As shown in figure 1.1(a), the streamlines are symmetric fore-aft and left-right. The flow field can (partly) be determined analytically (Batchelor, 1967), and typical streamlines close to the cylinder are shown in figure 1.1(a).

When the Reynolds number is increased to the range $5 \lesssim \mathrm{Re} \lesssim 40$ the fore-aft symmetry is broken as separation of the streamlines takes place on the cylinder's lee-side and attached zones of recirculating fluid form as sketched in figure 1.1(b). The left-right symmetry is retained, rendering the attached eddy on the left (right) side a positive (negative) sense of rotation. No complete theory exists for the steady flow field in this case, and experiments as well as simulations are needed to study this flow. For example, observations in a water tank (Taneda, 1956) and numerical simulations of the flow field (Brøns *et al.*, 2007) show a linear growth with Re of the

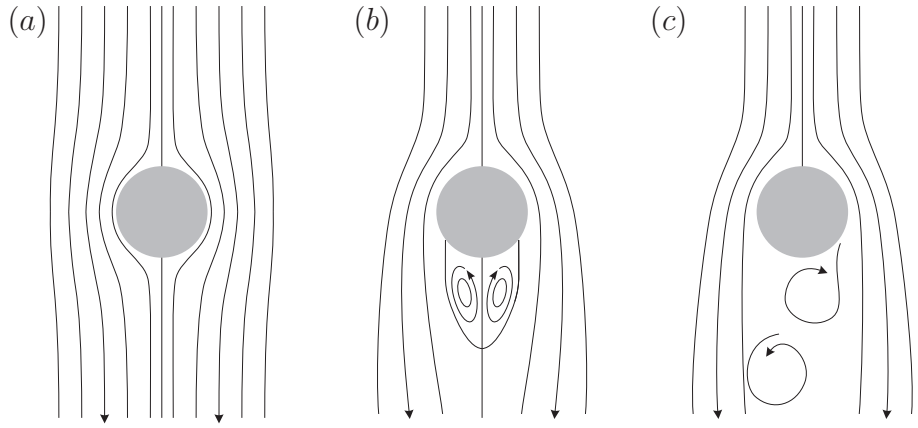

Figure 1.1: Depending on the Reynolds number, three different types of flow patterns are formed around a solid cylinder as the fluid moves from top to bottom. For small Reynolds number, the creeping flow is symmetric left-right and fore-aft (a). At larger Reynolds number the fore-aft symmetry is broken and stationary zones of rotating fluid, attached vortices, sit on the lee-side of the cylinder (b). For yet larger Reynolds numbers the vortices are shed successively into the wake, forming a periodic vortex wake (c), that can be three-dimensional and turbulent.

eddy's streamwise length.

The third and perhaps most fascinating flow is found as Re is increased to the range $40 \lesssim \mathrm{Re} \lesssim 180$. The flow, sketched in figure 1.1(c), is now unsteady as the eddies on the cylinder's lee side detach one after the other such that one eddy shed has the opposite sense of rotation compared to the previously shed eddy. As they are washed downstream, they form a vortex wake structure like a staggered grid of vortices, as shown in the photograph in figure 1.2(a). Here, the vortices on the left rotate counterclockwise and the vortices to the right rotate clockwise. This regime of Reynolds number is what Karl Hiemenz considered, and the wake type is indeed the von Kármán vortex wake. In this range of Re the vortex shedding is two-dimensional and laminar (Williamson, 1996).

For higher Reynolds numbers, $\mathrm{Re} \gtrsim 260$ the flow is three-dimensional as turbulence becomes increasingly more dominant in the region of flow close to the cylinder. A few cylinder diameters downstream a vortex wake with a structure similar to the von Kármán wake emerges from the turbulent flow, and therefore the von Kármán wake is ubiquitous in nature. Examples can be seen behind bridge pillars in a river and even in low cloud covers advecting over mountaneous islands such as the Aleutian Islands close to Alaska.

Vortices are shed with a well-defined frequency. The wake frequency f_n, which

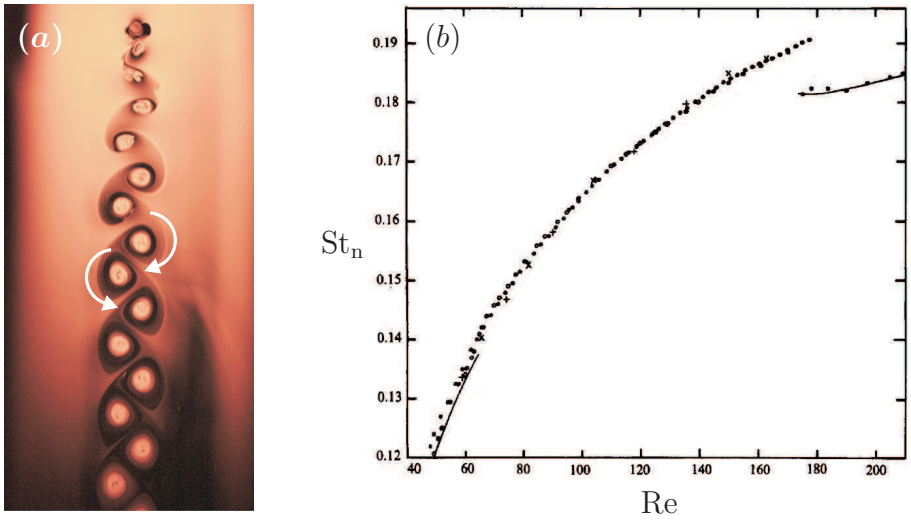

Figure 1.2: The classical von Kármán wake as seen in the soap film tunnel (a). Arrows indicate the direction of rotation for vortices on each side of the wake. Measured 'universal' relationship between $\mathrm{St_n}$ and Re for parallel vortex shedding behind a stationary cylinder (b). The discontinuity at $\mathrm{Re} \sim 180$ is due to three-dimensional effects in the wake. The figure is from Williamson (1989) and modified to highlight the measurements.

is half the vortex shedding frequency, together with the cylinder diameter, D, and flow speed U combines to the dimensionless *Strouhal number*

$$\mathrm{St_n} \equiv \frac{D f_\mathrm{n}}{U}. \tag{1.2}$$

Figure 1.2(b) shows measured values of $\mathrm{St_n}$ vs. Re in settings where the vortex shedding is ensured parallel to the cylinder span with clever manipulation of the flow at the cylinder ends (Williamson, 1989). In this case the flow is therefore close to two-dimensional. At $\mathrm{Re} \sim 50$ the vortex shedding takes place such that $\mathrm{St_n} \sim 0.12$. $\mathrm{St_n}$ gradually increases with Re until three-dimensional effects in the wake lead to a discontinuity in the Strouhal-curve at $\mathrm{Re} \sim 180$. At $\mathrm{Re} \gtrsim 500$ (not shown in the figure), $\mathrm{St_n}$ settles to the constant value ~ 0.21 over a broad range of Re. Due to the periodic flow and pressure fields close to the cylinder, it feels periodic drag and lift forces that can induce oscillations (Williamson & Govardhan, 2004). Hence, for engineering structures such as bridge pillars, off-shore oil-pipes, bridge cables and even buildings, it is important that vortex-induced resonant vibrations are avoided. In the opposite case, vibrations can lead to structural breakdown.

Many un-answered questions about the von Kármán wake exist. For example, no complete theoretical explanation for the relation between $\mathrm{St_n}$ and Re has been

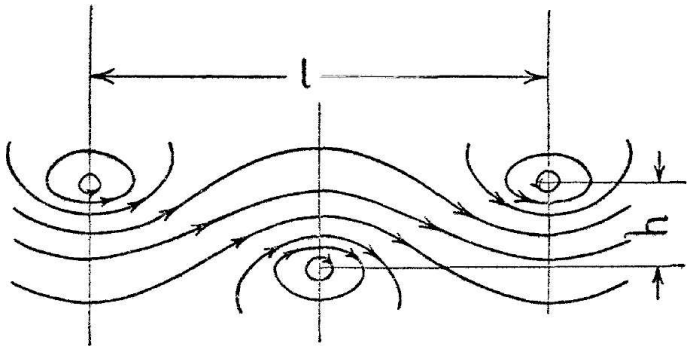

Figure 1.3: Von Kármáns original sketch of a vortex wake section in his analysis (von Kármán, 1911a,b). The full wake is the infinite extension sideways of the section shown.

put forward. A historically important relation, based on measurements, was put forward by Roshko (1954) as

$$\mathrm{St_n} = A\left(1 - \frac{B}{\mathrm{Re}}\right), \tag{1.3}$$

where A and B are constants. For instance in the range $40 \lesssim \mathrm{Re} \lesssim 180$, $\mathrm{St_n} = 0.212(1 - 21.2/\mathrm{Re})$ and in the range $\mathrm{Re} > 180$, $\mathrm{St_n} = 0.212(1 - 12.7/\mathrm{Re})$. An emphirical $\mathrm{St_n}$-Re relationship of the above form is supported by observations of the vortex roll-up, and order-of-mangitude estimates of the terms in the vorticity transport equation (Ponta & Aref, 2004). Recent careful analysis (Williamson & Brown, 1998) of direct numerical simulations of the flow past the cylinder (Henderson, 1997) reveal that in fact a better representation of the $\mathrm{St_n}$-Re curve is obtained by a series in $1/\sqrt{\mathrm{Re}}$, i.e.,

$$\mathrm{St_n} = A + \frac{B}{\sqrt{\mathrm{Re}}} + \frac{C}{\mathrm{Re}} + \ldots \tag{1.4}$$

Here, Williamson & Brown (1998) show that the fitting error of equation (1.4) is one order magnitude smaller than the expression in equation (1.3).

A characteristic of the von Kármán vortex wake is the geometry of the wake a few cylinder diameters downstream. This was first treated by von Kármán in 1911 (von Kármán, 1911a,b) who predicted, assuming the wake as infinitely long rows of point vortices in an ideal fluid (figure 1.3), an equilibrium wake structure when the two vortex rows are either symmetric or perfectly staggered. From his analysis, the symmetric configuration turned out linearly unstable. The staggered configuration, however, turned out neither linearly stable nor linearly unstable provided that the

geometry of the wake satisfied

$$\cosh \frac{\pi h}{l} = \sqrt{2} \tag{1.5}$$

where, as shown in figure 1.3, the lateral distance between vortices of opposite sign is h and the streamwise distance between same-signed vortices is l. In the derivation of equation (1.5) it is assumed that the double rows are perfectly staggered, i.e., the streamwise distance between neighbouring vortices of opposite sign is $l/2$. Equation (1.5) gives $h \approx 0.28l$. Although the predicted wake geometry has been successfully created and found stable numerically, still to this day no point-vortex model has successfully explained the observed stability of the wake that haunted Karl Hiemenz a century ago.

The staggered row geometry, equation (1.5), was recently found numerically in a Bose-Einstein condensate that flows past a potential acting as obstacle (Sasaki *et al.*, 2010). In the study it was found that the potential produces a von Kármán like wake at carefully selected parameters. The wake found in the Bose-Einstein condensate differs in one important aspect from the wake in a 'real' fluid with finite viscosity, such as figure 1.2(a). In the ideal fluid of the condensate, the wake is comprised by *four* vortices in a periodic strip. Two-by-two the same-signed vortices orbit close to each other in place of the individual vortices identified in viscous fluids. From the geometrical center of the same-signed vortices, Sasaki *et al.* (2010) calculated the geometry of the wake as $h = 0.28l$ in agreement with von Kármán's prediction.

1.2 Wakes of an oscillating cylinder

A rich variety of wake structures are found when the cylinder is forced to oscillate in the uniform free streaming flow. Perhaps the most celebrated work on this problem is that of Williamson & Roshko (1988) (and recently re-visited by Morse & Williamson (2009)), who considered a cylinder that is driven along a sinusoidal trajectory through still water. This situation is analogous to oscillating the cylinder transverse to a uniform free flow. They found simple and periodic (i.e. von Kármán) wakes as well as complicated wakes, where several vortices are shed in each period of oscillation. Two of the experimental images are seen in figure 1.4. (a) shows a wake type different to the von Kármán wake in the sense that the counter-rotating vortices are almost aligned on a single row. (b) shows a wake type where two pairs of vortices are formed in each oscillation period.

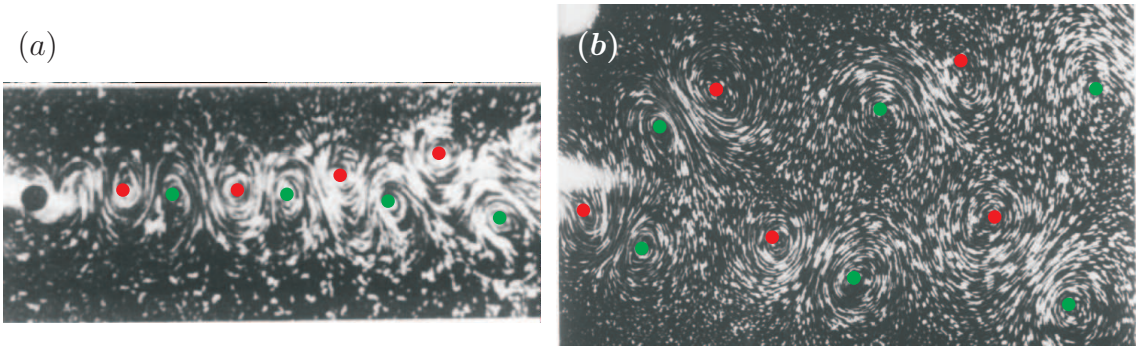

Figure 1.4: Examples of the vortex wake behind a cylinder that moves along a sinusoidal trajectory in otherwise quiscent water. Aluminium particles sprinkled on the free surface reveal the wake structure. (a) The cylinder sheds two vortices per oscillation period thereby forming a von Kármán wake ($2S$). (b) four vortices organised as two pairs ($2P$) are shed per period. The cylinder moved from right to left and it has just exited the picture. Green (red) dots mark vortices with a positive (negative) sense of rotation. The pictures are from Williamson & Roshko (1988).

Using a symbolic code of numbers and letters, Williamson and Roshko constructed a map, figure 1.5, of periodic vortex wakes spanned by the oscillation period and transverse amplitude. In their terminology 'S' is short for 'single vortex' and 'P' is short for a 'pair of vortices'. A von Kármán wake is therefore labeled '$2S$' and a wake that is comprised of two vortex-pairs shed per oscillation period is labeled '$2P$'. It is interesting to note from the wake map, that despite the symmetry of the experiment, in the sense that the cylinder moves along a sinusoidal trajectory in otherwise still fluid, they observed asymmetric wakes. The $P+S$ wake, for example, is comprised by a vortex pair on one side and a vortex singlet on the other side of the center-line.

Williamson and Roshko identified in the 'fundamental lock-in region' how shear layers on each side of the cylinder roll up as the cylinder experiences large accelerations. Thereby, four 'regions of vorticity' are formed each period. Depending on the timing between formation and shedding of these regions they explain qualitatively the location of regions of $2S$ and $2P$ wakes.

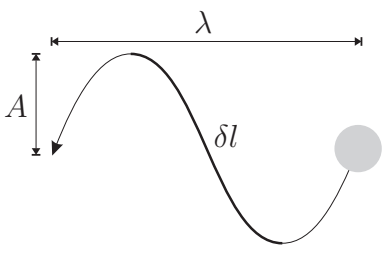

As the trajectory wavelength and/or amplitude is increased, wakes with a larger number of vortices per oscillation period are shed. This trend is explained in simple terms by Ponta & Aref (2005) who considered the cylinder trajectory with wavelength λ and amplitude A as shown to the right. They then compared the length, δl, of the section

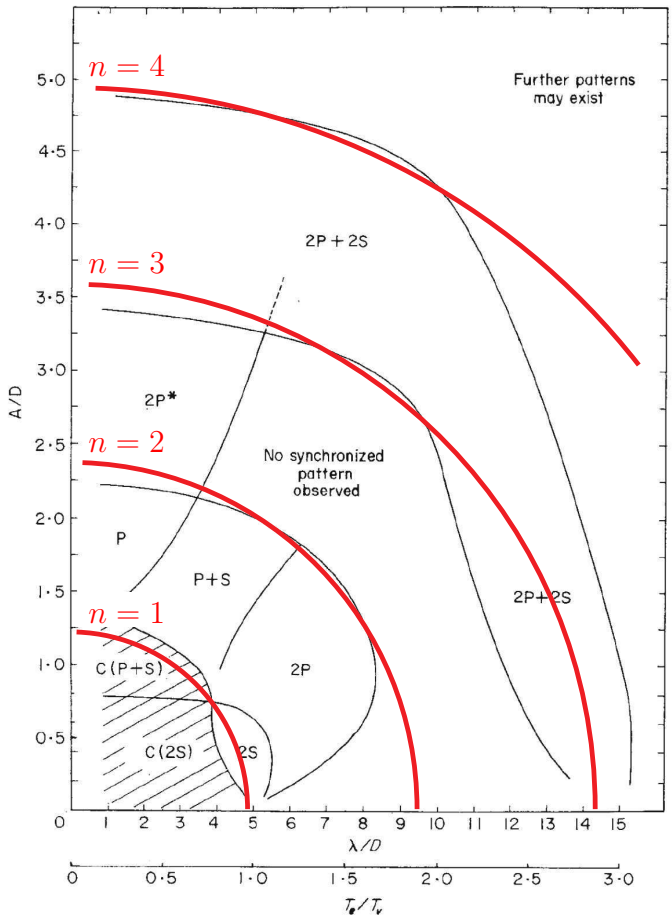

Figure 1.5: Map of vortex wakes found behind a cylinder that oscillates transverse to a free streaming flow (Williamson & Roshko, 1988). Red, circular lines are contours that explain borders between regions of different wake types (Ponta & Aref, 2005).

joining the two extreme positions of the trajectory with the streamwise distance (times an integer n) between neighbouring vortices shed by a stationary cylinder, i.e.,

$$\delta l = n\frac{U}{2f_{\mathrm{n}}}. \tag{1.6}$$

For $n = 1, 2, \ldots$ the condition gives an implicit relation between the trajectory wave length λ and the amplitude A. Equation (1.6) gives the circular contours, for some n, shown in figure 1.5 that approximates well the boundaries between regions of different wake types. The higher n, the more vortices are shed in each oscillation period which is also observed in the experiment.

1.3 Wakes of swimmers

A flying bird or a swimming fish are examples from biology where a flow is actively modified through oscillatory motion of a body. Whereas the wing of a bird in addition to thrust production also provides the necessary lift to keep the creature aloft, the tail of a fish is exclusively designed to produce effective thrust and to manoeuver.

Typically, a fin or wing flaps in a combination of a purely linear *heaving* motion, y, and a purely rotational *pitching* motion, ϕ, cf. figure 1.6. The motion of the foil is thus expressed by

$$y(t) = y_0 \sin(2\pi f t) \tag{1.7a}$$

$$\phi(t) = \phi_{\mathrm{m}} + \phi_0 \sin(2\pi f t + \psi) \tag{1.7b}$$

where ϕ is the foil angle relative to the cruising direction (Triantafyllou *et al.*, 2004). The motion of the foil is often expressed by the amplitude-based *Strouhal number*,

$$\mathrm{St}_A \equiv \frac{2Af}{U} \tag{1.8}$$

where f is the flapping frequency, $2A$ is the wake width, which for simplicity often is taken as the foil tip excursion lateral to the cruising velocity with magnitude U. Notice that St_A accounts for both the flapping frequency and amplitude. For fish it is well established that the optimal mechanical efficiency (defined as the ratio of propulsive power to input power) takes place when the ratio y_0/C (C is the foil chord) is ~ 1, the amplitude-based Strouhal number is in the range $0.25 \leq \mathrm{St}_A \leq 0.35$, and the pitching motion leads the heaving motion by $\psi = 75°$ (Anderson *et al.*, 1998). These findings are in agreement with observations of swimming fish (Triantafyllou, 1993) as well as birds (Taylor *et al.*, 2003).

Studies of flapping foils often express the foil kinematics by dimensionless numbers that account separately for the flapping frequency and amplitude. These are dimensionless frequency, the Strouhal number,

$$\mathrm{St}_D \equiv \frac{Df}{U}, \tag{1.9}$$

where D is the width of the foil. The flapping amplitude is expressed by the dimensionless flapping amplitude

$$A_D \equiv \frac{2A}{D}, \tag{1.10}$$

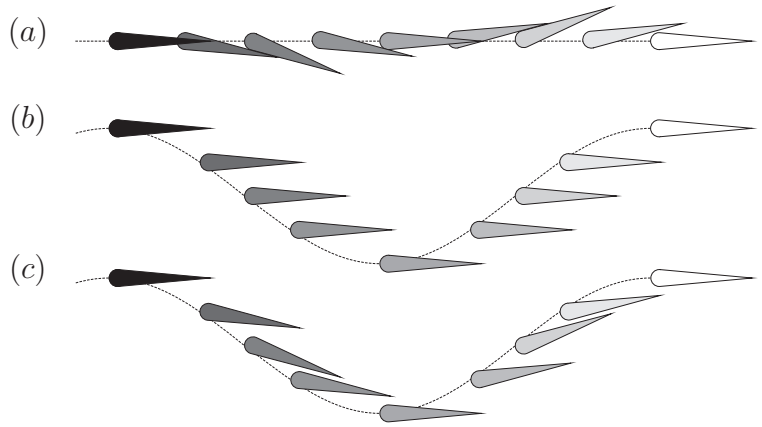

Figure 1.6: Different flapping modes of a foil that moves leftwards along the dotted line. (a) is the purely pitching node, (b) is the purely heaving mode and (c) is a combination of the two.

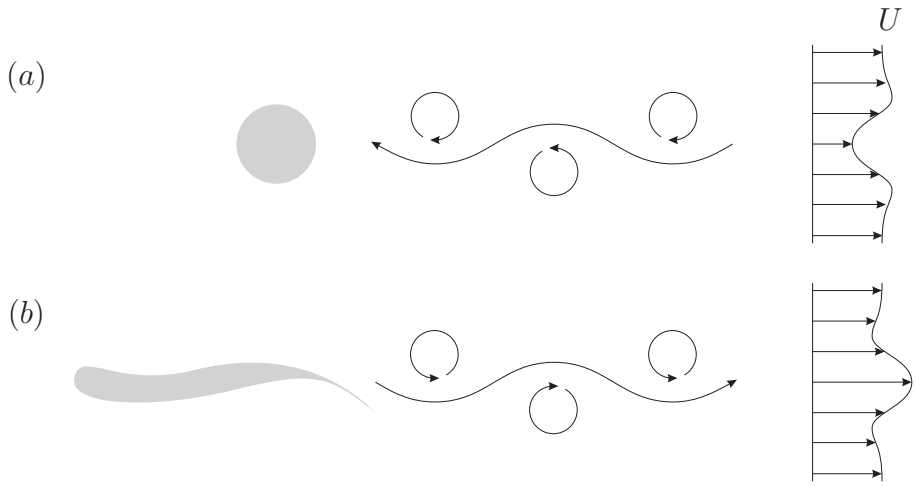

Figure 1.7: The von Kármán wake of a cylinder that experiences drag (a) and the inverted von Kármán wake of a swimming fish that produces thrust (b). In the mean flow speed through a line perpendicular to the overall flow directed left-to-right, the vortex wakes give rise to a velocity deficit (indicating drag) or a velocity excess (indicating thrust).

where $2A$ is the total horizontal excursion of the foil tip, as above. Notice that by definition, $\mathrm{St}_A = \mathrm{St}_D \cdot A_D$.

An interesting question regarding flapping foils is the link between vortex wake structure and streamwise forces on the foil.

The wake of a swimming fish has a close resemblance to the von Kármán wake, except that the individual vortices have an opposite sense of rotation. A simple idea of the streamwise fluid forces is given if we consider figure 1.7. Think of the wake as two rows of spinning wheels that advect fluid. Behind the cylinder the vortices spin such that momentum is advected upstream, towards the cylinder as

shown in (*a*). In a mean-flow profile, this is reflected in a reduced velocity on the center-line, which again indicates the drag experienced by the cylinder. Behind the swimmer, as shown in (*b*), momentum is transported away from the swimmer which gives the mean flow a jet-like profile. The latter *inverted* von Kármán wake type indicates the production of thrust and it has been measured behind steadily swimming fish such as the mullet (Müller *et al.*, 1997) and bluegill sunfish (Drucker & Lauder, 1999). Notice that the 'real' wake of a swimming fish or the wake of a foil with limited aspect ratio is three-dimensional. Consequently, vortex lines have to form closed loops or terminate on a solid structure. Indeed, the inverted von Kármán wake revealed by measuring the flow in a single plane, as obtained from conventional particle image velocimetry (PIV), is in fact composed of vortex rings linked together (Drucker & Lauder, 1999). Detailed studies of flapping finite-span wings reveal intricate interaction of interconnected vortex tubes formed at the foil's leading and trailing edge as well as the side of the foil at $\mathrm{Re} = 164$ (Ellenrieder *et al.*, 2003; Buchholz & Smits, 2008). Although the flow at higher Reynolds numbers is more turbulent, the processes involved in production of circulation and formation of vortex tubes is presumably similar.

von Kármán & Burgers (1963) support this interpretation with ideal flow theory. They predicted the transition from drag to thrust of a heaving plate to take place exactly as the von Kármán wake transits to an inverted von Kármán wake. In the intermediate case, the vortices are aligned on the center-line of the system, whereby they cancel each other in the mean flow. Garrick (1936) found from inviscid theory the streamwise forces on a flat plate that performs simple harmonic pitching oscillations around its leading edge. The plate has a chord length C and it is held in position as an incoming flow of free stream flow speed U is imposed. He determined the transition from drag to thrust to be independent of the pitching oscillation amplitude, and occur at a frequency $f = U/(3.16\ C)$. As we will show in chapter 4, the transition from drag to thrust generally cannot be predicted by the flapping frequency alone.

1.4 Selected work on wakes behind flapping foils

A large body of work exists on the wake structures behind foils that oscillate in either a pitching, heaving or combined manner cf. equation (1.7) (Triantafyllou *et al.*, 2004). This section presents a short review of experimentally measured wake structures behind foils that oscillates in either of these modes. The motivation to

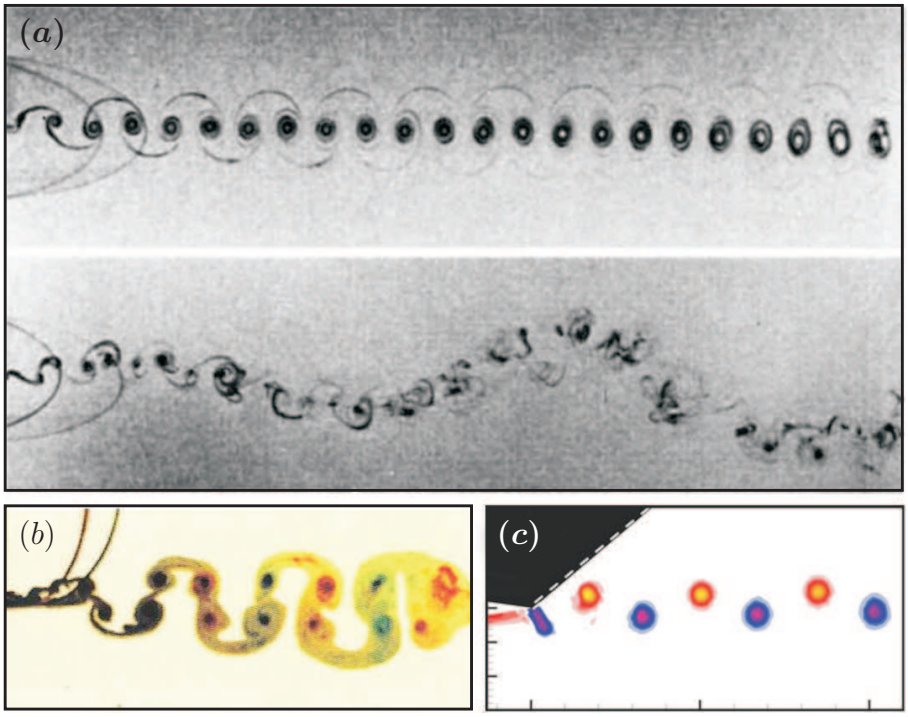

Figure 1.8: Selected visualisations of periodic vortex wakes of a flapping foil as the fluid moves from left to right. Shown are the von Kármán wake and undulating von Kármán wake measured by Koochesfahani (1989) (a), a $2P$ wake measured by Lai & Platzer (1999) (b), and the inverted von Kármán wake measured by Bohl & Koochesfahani (2009) (c).

study these systems comes from both industrial applications such as wings exposed to an unsteady wind, fluttering airfoils as well as biological systems where wings or fins are used as propulsors or to manoeuver.

Bratt (1953) used smoke to visualise wake structures of a rigid, pitching NACA 0015 airfoil in a wind tunnel. By varying the Reynolds number in the range $4 \cdot 10^3 \lesssim \mathrm{Re} \lesssim 5 \cdot 10^5$, he found von Kármán wake and inverted von Kármán wakes, and he even reported an apparant $2P$ wake type although it was 'hard to reproduce'. Koochesfahani used dye in a water channel to visualise the vortex wakes of a pitching NACA 0012 that performs pitching oscillations around the leading 1/4 chord (Koochesfahani, 1986, 1989). By varying oscillation frequency and amplitude, he observed von Kármán wakes (figure 1.8(a)), inverted von Kármán wakes and $2P$ wakes. For low pitching frequency and amplitude, Kooochesfahani measured an 'undulating von Kármán wake', a wake where several vortices are distributed along a wavy, narrow band that reflects the oscillatory motion of the foil (figure 1.8(a)). Their set-up did not allow the latter wake type to be characterised in the terminology of Williamson-Roshko. Introducing a slight asymmetry in the pitching motion

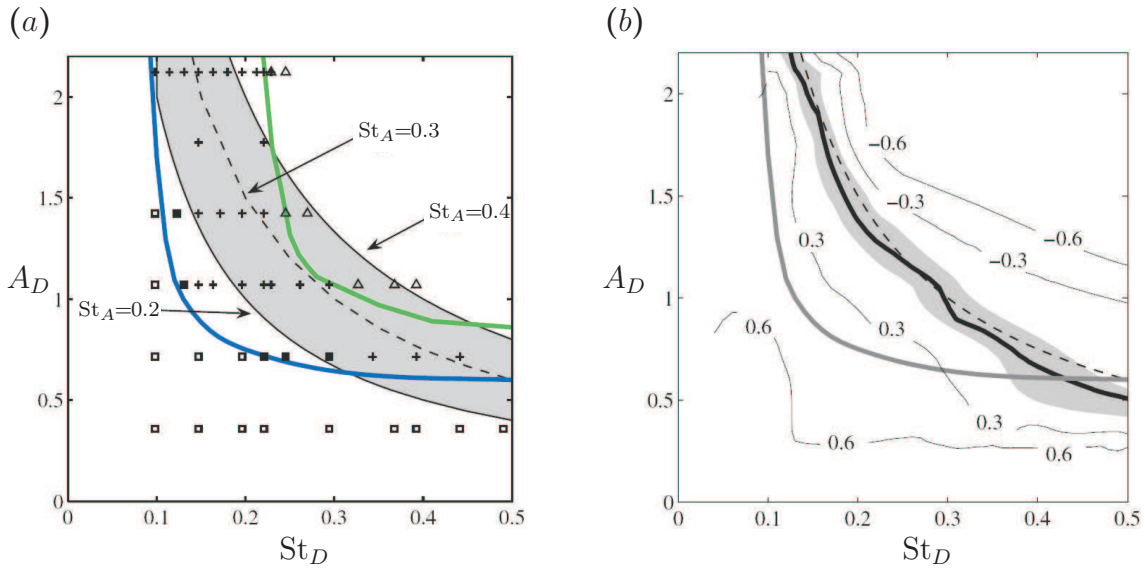

Figure 1.9: The main results of Godoy-Diana *et al.* (2008). (*a*) shows the measured wake types which are von Kármán wakes (open boxes), aligned $2S$ wake (filled boxes), inverted von Kármán wake (plus) and oblique inverse von Kármán wake (triangles). Blue and green lines are hand-drawn boundaries between the different wake types. (*b*) shows contours of the mean drag coefficient where the transition from drag to thrust is along the thick black curve and thrust takes place in the upper-right part of the map. The figure is from Godoy-Diana *et al.* (2008).

waveform, Koochesfahani found asymmetric $P + S$ wakes as well. The Reynolds number is Re = 1440, based on foil width D and the free stream flow speed U. Recently, Bohl & Koochesfahani (2009) again considered the NACA 0012 foil that pitches in a simple harmonic fashion in flowing water at Re $\sim$ 1500. They made use of molecular tagging velocimetry to extract, in high spatial resolution, the vorticity field and vortex wake structure. Special focus was on wakes of the von Kármán type. By varying the oscillation frequency only they found from a control volume analysis taking into account pressure variations in the wake, that the wake transits to an inverted von Kármán wake before the transition from drag to thrust. An example of the inverted von Kármán wake measured by Bohl & Koochesfahani is shown in figure 1.8(*c*).

Recently Godoy-Diana *et al.* (2008) measured $2S$ wakes behind a pitching foil in a water tunnel at Re = 255 and supplemented their wake measurements with propulsive forces. The latter was obtained from PIV measurements of the mean flow and a subsequent momentum balance through a control volume enclosing the foil. The discrete data points, 52 combinations of pitching frequency and amplitude, were compiled in a wake map (figure 1.9(*a*)) spanned by St_D and A_D in the ranges

$0 \leq \mathrm{St}_D \leq 0.5$ and $0 \leq A_D \leq 2.1$. From the wake map they concluded that the transition from von Kármán wake to inverted von Kármán wake generally precedes the transition from drag to thrust, figure 1.9(b). The work of Godoy-Diana *et al.* (2008) gave an overview of the vortex wake structures and associated forces behind the pitching foil. However, the resolution in their wake map as well as limitations in resolving smaller structures in the flow prevented a clear identification of the actual wake structure as well as the boundaries between regions of different wake types. Futhermore, Godoy-Diana *et al.* (2008) find for selected flapping parameters that the foil can produce a mean thrust while leaving behind a von Kármán wake.

Lai & Platzer (1999) used dye visualisation to reveal von Kármán wake, inverted von Kármán wake and $2P$ wake (figure 1.8(b)) behind NACA 0012 foils that performs heaving oscillations at selected parameters in a water channel. Varying flapping amplitude and frequency of the oscillation, they found the transition from von Kármán wake to inverted von Kármán wake to take place as the non-dimensional heave velocity $kh = 0.4$, which corresponds to $\mathrm{St}_A = 0.13$.

Lentink *et al.* (2008) studied the wake structure of a biologically inspired setting where a foil oscillates in a combination of heave and pitch at fixed amplitude $A_D = 15$ and $0.0042 < \mathrm{St}_D < 0.25$. In a soap film flow they measured simple von Kármán wakes, $2P$ wakes, asymmetric P+S, $2P$+S, $3P$+$2S$ wakes and aperiodic wakes (for low oscillation frequency) at $\mathrm{Re} \sim 800$. They had special focus on the formation vortices at the foil's leading and trailing edge, which was observed to take place when $\mathrm{St}_D \gtrsim 0.008$. After shedding, these vortices formed a pair in the wake. Two such pairs could form during one flapping period. Lentink *et al.* (2008) then compiled the vortex wakes in a diagram showing that more vortices were shed per flapping period as St_D decreases. It is interesting to note that Lentink *et al.* (2008) found mostly asymmetric and even aperiodic wakes which contrasts the previous studies Bratt (1953); Godoy-Diana *et al.* (2008); Koochesfahani (1989); Bohl & Koochesfahani (2009). Based on our experience with periodic wakes, we believe that the asymmetric wakes measured by Lentink *et al.* (2008) is due to their asymmetric mechanical drive.

The wake structure of and associated forces on oscillating foils in the intermediate Reynolds number range 10^2 to 10^5 have thus been studied in both experiments, theory and numerical simulations for almost a century. Studies in the existing literature are usually carried out for a few selected values in, say, frequency or amplitude of the oscillation. This has produced a body of work on oscillating foils that is quite extensive, although it is somewhat scattered in the parameter space spanned

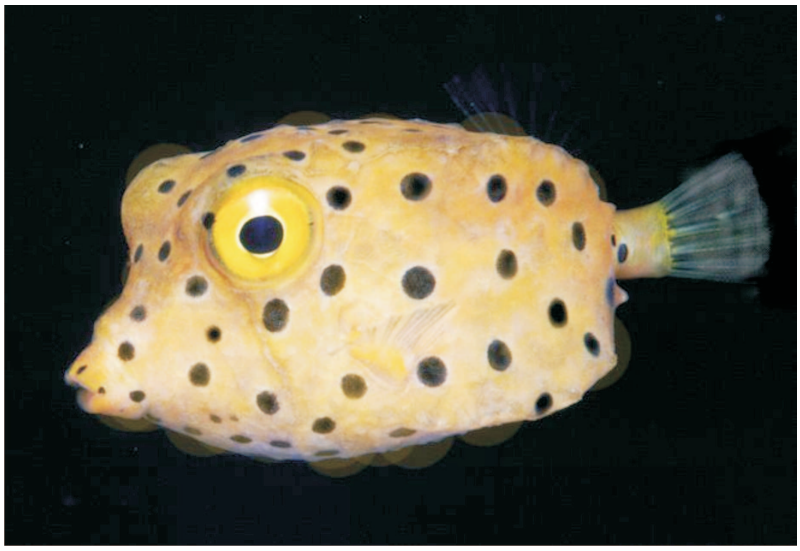

Figure 1.10: A juvenile yellow box fish (*Ostracion cubicus*) utilises a purely pitching posterior fin to swim and manoeuver. Credits: Jeff Jeffords, with permission.

by oscillation frequency and amplitude. In this dissertation we will present a more thorough study of the vortex wake structures of and fluid forces on a pitching foil, in the space spanned by $0 < \mathrm{St}_D < 0.3$ and $0 < A_D < 2$.

As an ending remark it is mentioned that in nature, propulsion by means of a purely pitching foil is named the *ostraciiform* mode of swimming. It is employed for rapid escape events by fish such as the peculiar boxfish shown in figure 1.10 (Hove *et al.*, 2001). The ostraciiform mode of swimming is recognised to yield high maneuverability (Blake, 1981).

1.5 Thesis outline and main results

The formation of periodic vortex wakes is a central theme of this dissertation—predominantly the formation of vortex wakes by a foil that undergoes a prescribed motion. As suggested, the parameters that describe flapping motion in biology are many. Besides the flapping frequency, phase and amplitude of heave and pitching motions, the system is characterised by foil geometry and flexibility, properties of the fluid in which the body moves, and the cruising speed. In order to restrict the parametric space, most work presented in this dissertation consider rigid foils with a fixed geometry. The foil performs simple harmonic pitching oscillations only, which corresponds to $y_0 = \theta_\mathrm{m} = 0$ in equation (1.7).

The dissertation is organised in 7 chapters, of which chapters 1 and 2 are introductury and they are predominantly based on existing literature. Chapters 3–7 consist of results obtained as part of this ph.d. The dissertation and main results are outlined in the following.

In chapter 2 an introduction to soap films and in particular aspects of their surface tension properties are given. The use of a soap film as a tool for flow visualisation experiments is discussed, and an experimental set-up that makes use of a vertically flowing soap film to produce quasi two-dimensional flow is described. Finally, the effective viscosity of soap films and in particular the soap film used for flow visualisations in the present work is measured experimentally and discussed.

Chapter 3 introduces an experimental investigation of the vortex wakes formed by a rigid foil that performs prescribed simple harmonic pitching oscillations in a uniform free streaming flow. A measured 'map of vortex wakes' in the space spanned by (dimensionless) pitching frequency and amplitude is presented. The map of vortex wakes is dominated by wake types where two vortices are shed from the foil per oscillation period, but more complicated wakes also exist. For example, in the range of low Strouhal number, periodic wakes comprised by up to 16 vortices formed per oscillation period were measured. This observation is explained by a simple model that treats the foil as a passive source of circulation. It is shown how two disconnected regions of $2P$ wakes exist in the wake map and it is explained through a detailed study of the $2P$ wake formation. Here, distinct sources of circulation on the foil are identified as the foil's leading edge and its sharp trailing edge. These sources form four regions of vorticity per flapping period, and it is shown how these regions develop into distinct vortices to form a $2P$ wake.

The major results in this chapter are published in Schnipper, Andersen & Bohr: *Vortex wakes of a flapping foil*, Journal of Fluid Mechanics **633**, 411–423 (2009), and Andersen, Bohr & Schnipper: *Separation vortices and pattern formation*, Theoretical and Computational Fluid Dynamics **24**, 329–334 (2010).

In chapter 4, the measured map of vortex wakes is compared with a similar map obtained from numerical simulations of a two-dimensional incompressible and Newtonian flow past the pitching foil, in conditions matching those in the experiment. Simulations were carried out on a regular grid, comprised of 1000 simulations, in the same parameter space as measured. The measured and simulated wakes show impressive quantitative agreement, and the boundary layer evolution and vortex for-

mation are qualitatively similar. The simulated streamwise forces on the foil show that the transition from von Kármán wake to inverted von Kármán wake precedes the transition from drag to thrust, and both transitions are well fitted by lines of constant amplitude-based Strouhal number. The simulated unsteady and mean forces are discussed in relation to values obtained from a quasi-static model. The model describes the transition from drag to thrust fairly well, but fails to predict the correct phase relative to the foil rotation angle.

Chapter 5 presents an experiment where the foil pitches in an otherwise quiescent soap film. The impressive flow due to the pitching foil is shown in a single image that reveals how two vortical lobes form each oscillation period. The lobes pile up and ultimately form a large region of active flow that has the shape of a pair of butterfly wings.

The image is published in Schnipper, Tophøj, Andersen, and Bohr: *Japanese Fan Flow*, Physics of Fluids **22**, 091102 (2010).

In chapter 6, experiments on the swimming speed due to a pitching foil are described. An experiment has been devised, where a foil undergoing prescribed pitching motion while free to swim along a fixed path in a water tank. The three-dimensional foil is swimming at a speed given entirely by the fluid forces acting on the foil. The chapter consists of preliminary results that show how the foil's swimming speed increases linearly with the pitching frequency, above some threshold set by static friction in the system.

Chapter 7 presents experiments on interacting tandem flappers in an open flow. In a vertically flowing soap film tunnel a rubber filament, a flapping flag, models a passive 'swimmer'. Downstream of the flag objects of three different types are introduced, one at a time: A rigid plate, a plate performing prescribed pitching oscillations and a flag identical to the leader. Generally, the flag is affected by its downstream neigbour such that the flag experiences a reduced drag compared to the drag it feels when it is left alone in the same flow. It is shown that the observed frequency synchronisation of two tandem flappers is not limited to cases of passively flapping bodies: By actively flapping a plate in the wake, it is possible to make the upstream flag lock to the forcing frequency over a broad range of frequences. The results are discussed in relation to animals such as schools of fish or a predating fish chasing its prey.

The work presented in this chapter was conducted during a 4 month stay with Jun Zhang at the Applied Mathematics Laboratory, New York University.

Throughout the dissertation, physical units are kept in the cgs system, i.e., length is measured in ‘cm’, mass in ‘g’, time in ‘s’.

Chapter 2

Soap films and two-dimensional flows

Soap films are excellent to visualise overall features as well as minute details of two-dimensional flows. The first documented work that makes use of soap films to visualise flows is that of Sir James Dewar in 1923, who visualised the flow due to a jet of air impingning on a horizontal soap film suspended on a wire frame (Dewar, 1923). Later on, in the early 1980s, soap films gained widespread popularity as a flow visualisation tool. Of particular importance is the inspirational work of Yves Couder and co-workers, who studied wakes of cylinders that penetrates the horizontal and otherwise quiescent soap film (Couder & Basdevant, 1986). Gharib & Derango (1989) invented a 'liquid film tunnel' where a planar water jet pulls a soap film and thereby produces a horizontally moving soap film in which a number of experiments which shear flows were conducted. Kellay *et al.* (1995) made a simpler version where gravity drives the flow vertically downwards between two guide wires. In the last two decades, several groups have adopted gravity-driven soap film tunnels to study a great variety of phenomena such as the shedding of vortices behind a cylinder in an otherwise uniform flow (Vorobieff & Ecke, 1999a,b), structure in two-dimensional turbulence (Rivera *et al.*, 1998; Rutgers, 1998), flapping of flags (Zhang *et al.*, 2000), passive 'swimming' of a filament behind a cylinder that sheds a von Kármán wake (Jia & Yin, 2009) and the 'inverted drafting' of two flags that flap in a tandem configuration (Ristroph & Zhang, 2008).

This chapter first gives a general introduction to soap films. Part of the content is based on the books by Isenberg (1992) and Boys (1890), that both thoroughly explains many aspects of soap films in an easy-to-digest language. Secondly, an experimental set-up that makes use of a flowing soap film to visualise two-dimensional

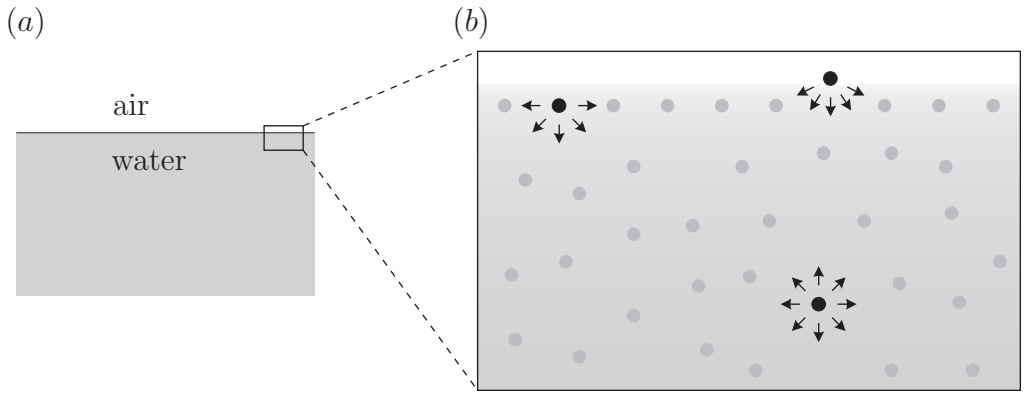

Figure 2.1: A free surface of water at rest (a). Molecules at the free surface feel an average force from their neighbours that is directed towards the bulk, whereas molecules in the bulk feel a zero average force (b).

flows is presented. The flow tunnel is build as a part of this ph.d., and it will be used in chapter 3 to map out vortex wakes behind a flapping foil. A similar soap film tunnel is used in chapter 7 to study interaction of tandem flappers. The relevant properties of the flow tunnel are given, and the link between measured thickness variations and the underlying flow in the soap film itself is discussed, as is soap film tunnels as a testing ground for experiments on two-dimensional incompressible Newtonian flows.

2.1 Anatomy of a soap membrane

A solution consisting of soap and water can form thin fluid membranes suspended on, say, a closed loop like the wands used by children to blow bubbles. Typically, a simple solution of water and commercially available detergent produces films that persist for ~ 30 seconds. It is the soap molecules that enable the fluid to form thin, durable membranes. It seems that Dewar (1927) holds the record in long lasting soap membranes: In a sealed jar he was able to keep a circular soap film (diameter 19 cm) for 3 years!

Consider a volume of pure water at rest with the upper surface exposed to the air, as shown in figure 2.1(a). A tiny volume near the free surface showing the individual water molecules is shown in figure 2.1(b). Water molecules are polar and thus interact with each other as they ramble about due to thermal kinetic energy. A molecule in the bulk of the fluid will feel a zero force on average since it is surrounded by its identical neighbours. A molecule on the surface, however, only feels its neighbours on the surface and in the bulk fluid. The asymmety leads to

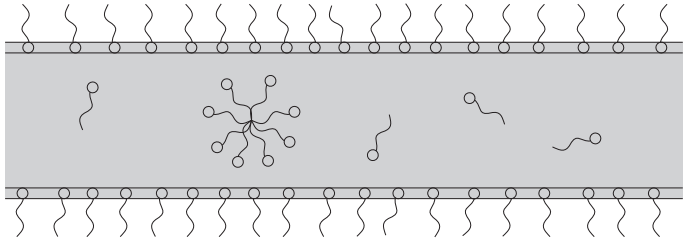

Figure 2.2: Anatomy of a soap film: Evenly spaced soap molecules on the surface reduce the surface tension of the solvent (water). Superfluous molecules form spherical micelles in the interstitial fluid layer.

a net force that is directed towards the bulk. Opposing this net force is the fluid pressure due to the surface molecule being bombarded by molecules in the bulk. Consider now a perturbation of the flat surface, for instance by displacing upwards a single surface molecule, cf. figure 2.1(b). The attractive forces from the neighbours now have a stronger component directed towards the bulk, and the perturbation is thus eliminated. In other words, the water tries to minimise the free surface area, which is an effect particularly pronounced for water. This is the reason why insects like the water strider (Hu *et al.*, 2003) or rigid, dense bodies like paper clips can float atop a water surface.

When soap is added to water, the solution can form thin membranes, with typical thickness of order $\sim 10\ \mu$m. Soap molecules are hair-pin shaped with a characteristic hydrophilic head attached in the end of a hydrophobic tail such as the commonly used Sodium Dodecyl Sulfate, SDS, molecule ($C_{12}H_{25}SO_4Na$). When dissolved in water, a portion of the slender molecules will migrate to the fluid-air interface where they will be evenly distributed in such a way that the tails point away from the bulk fluid as shown in figure 2.2. The concentration of molecules at one film surface, Γ_1, is related to the concentration in the interstitial fluid layer, c_1, by

$$c_0 = c_1 + 2\frac{\Gamma_1}{h}, \tag{2.1}$$

where c_0 is the average soap concentration of the solution and h is the film thickness. The surface concentration is, for small values, linearly related to the bulk concentration

$$\Gamma_1 = Kc_1, \tag{2.2}$$

where the constant K has dimension length and is related to the specific soap (Chomaz, 2001). For SDS soaps $K \sim 4\ \mu$m (Couder *et al.*, 1989).

For large concentrations the linear relationship (2.2) no longer holds as the surface can occupy no more soap. Instead, the superfluous molecules form spherical *micelles* in the bulk by directing their tails towards the same point, figure 2.2. This takes place when c_0 is larger than the critical micelle concentration c_m. In this range, the surface concentration settles to a constant value as sketched on the graph to the right.

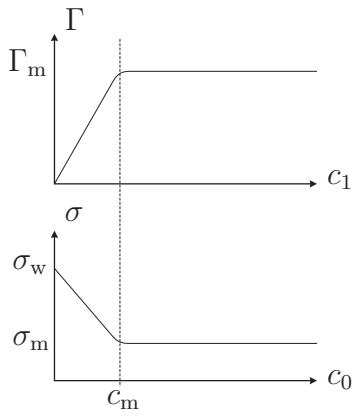

As soap molecules occupy space on the fluid surface, the surface density of water is lowered, which again lowers the surface tension of the solution to a value less than that for pure water σ_w. For small soap concentrations the surface tension departs linearly with Γ_1 from σ_w such that

$$\sigma = \sigma_\mathrm{w} - \Gamma_1 RT, \tag{2.3}$$

where R is the ideal gas constant and T is the temperature. Equation (2.3) is only valid for low concentrations of soap. When the critical micelle concentration is reached, no more soap molecules migrate to the surface, and σ accordingly attains the constant value c_m.

An interesting feature of soap films is the response to a sudden stretch. Here, soap molecules from the interstitial fluid layer have no time to migrate to the surface to ensure the equilibrium value of Γ_1 cf. equation (2.2). Thus, for a period of time, neighbouring soap molecules are moved further apart and in return the surface tension is increased cf. equation (2.3). As time evolves, soap molecules from the bulk of the film will migrate to the surface and equilibriate the surface soap concentration and surface tension. The surface tension before and after the applied stretch is generally not the same. The initial increase in surface tension is the *Marangoni* elasticity. On a long scale of time, soap migrates from bulk to surface to restore equilibrium concentractions cf. equation (2.3), and this long-term elasticity is the *Gibbs* elasticity. It should be noted that the time it takes soap to reposition from the interstitial fluid to the surface, τ, varies from $\tau = 0.01$ s (pure water and SDS solution) to $\tau = 1$ s when pollutants are present (Couder *et al.*, 1989; Chomaz, 2001). Isenberg (1992) quotes a factor 3 decrease in surface tension as a rule of thumb, and it is speculated that this value applies to 'standard' soap bubble solutions.

The special elastic property of soap films, the Marangoni elasticity, resists deformation thats would otherwise lead to rupture. Since pure water lacks this property,

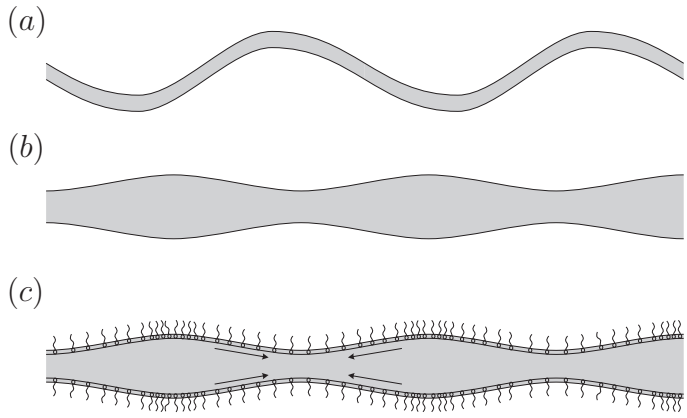

Figure 2.3: Three types of waves can propagate in soap films. (a) is the asymmetric (surface tension driven) waves, (b) is a symmetric (surface tension driven) wave, and (c) is a symmetric wave driven by Marangoni elasticity due to local stretching of the soap film surface.

it is not possible to blow bubbles of pure water.

Different types of waves can propagate in thin fluid films, sound waves and surface tension driven waves that deflect the film surface. Sound waves are longitudinal waves that propagate at the fluid's speed of sound, in soap solutions this is approximately the speed of sound in water, $1.5 \cdot 10^5$ cm/s. Since flows in soap films take place at velocities far smaller than the speed of sound, effects of compressibility are of no concern.

The surface tension driven waves are generally composed of either *asymmetric* or *symmetric* waves (Lucassen *et al.*, 1970). Taylor (1959) considered propagation of waves in thin water films and gave expressions for their velocities. The asymmetric wave, figure 2.3(a), is the sheet-analogy to a transverse wave on a string: The fluid film is deflected away from its resting plane and the surface is correspondingly stretched. Surface tension resists stretching and acts to restore the flat surface, and surface tension lets the asymmetric wave to propagate at a velocity that is independent on the wavelength. An expression for the propagation velocity is given in table 2.1. A value for typical soap films is $\sim$ 500 cm/s. This particular type of wave is the most commonly observed on soap films. Since the two liquid-air interfaces are displaced in phase, by the same amount, the asymmetric wave is not accompanied by a significant change in film thickness.

The symmetric wave, figure 2.3(b), is a longitudinal wave where the film thickness varies in such a way that the upper and lower surfaces are mirror images of each other. As for the asymmetric waves, surface tension is the driving mechanism. The propagation velocity for this type of wave depends on the wavelength and the

	Wave type	Propagation speed	Typical value
(a)	Asymmetric	$v_{\mathrm{as}} = \sqrt{\frac{2\sigma_f}{\rho h}}$	570 cm/s
(b)	Symmetric	$v_{\mathrm{sym}} = \frac{2\pi}{\lambda}\sqrt{\frac{\sigma_f h}{2\rho}}$	2.70 cm/s
(c)	Symmetric Marangoni	$v_{\mathrm{M}} = \sqrt{\frac{2E}{\rho h}}$	730 cm/s

Table 2.1: Propagation speed and typical values calculated for the different wave types shown in figure 2.3. The film considered has a thickness $h = 1.5$ μm, fluid density $\rho = 1.0$ g/cm^3, surface tension $\sigma_f = \frac{1}{3}\sigma_{\mathrm{w}}^{20°C} = 73$ g cm/s^2 and in case (b) waves of wavelength $\lambda = 0.1$ cm and in case (c) the Marangoni elasticity $E = 80$ g/s^2 (Couder *et al.*, 1989).

expression is seen in table 2.1. In soap films, symmetric waves can alternatively be propagated by the Marangoni elasticity. As the film becomes stretched in the nodes, a Marangoni flow is set up, which transports fluid along the film surface from the antinodes to the nodes. In soap films, the rate of change of thickness due to Marangoni driven waves dominate the conventional symmetric waves (Couder *et al.*, 1989). As we shall see later, the symmetric wave driven by Marangoni elasticity is the soap-film analogy to sound waves in air.

2.2 Thin film interferometry

Besides the ability to form stable membranes and bubbles, the soap film is appealing to the eye due to the many colours that are seen on a bubble as it floats in mid-air on a sunny day. The colours are due to interference in the film of varying thickness. In this section an explanation of the link between observed colours and film thickness variations is given.

Figure 2.4 shows a slab of soap film that is subjected to monochromatic light. As the incident ray of light I_1 meets the soap film, part of it ($\sim 96\%$) is transmitted through the air-liquid interface while the remainder reflects off the interface. After reflecting off the upper liquid-air interface ($\sim 4\%$), most of the remaining light is then transmitted through the lower surface, into the air as R_1. Similarly, the incident ray of light I_2 is partly reflected off the lower interface as R_2. The two rays R_1 and R_2 travel along the same path and an observer sees the resulting light as they interfere. Whether the interference is constructive og destructive depends on the soap film thickness.

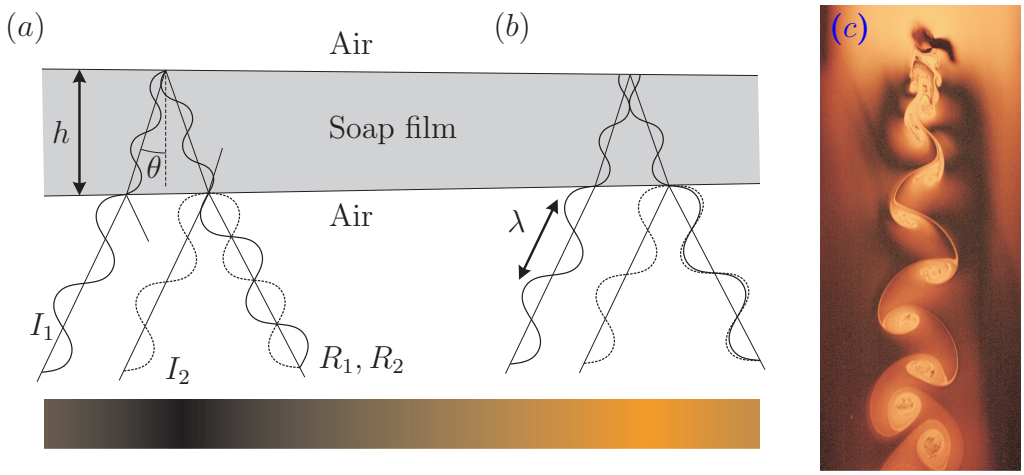

Figure 2.4: The incident ray of monochromatic light (I_1) is partly transmitted through the lower interface and partly reflected off the upper interface, before leaving the soap film downwards as R_1. Here it interferes with R_2 which is the part of I_2 that reflects off the air-liquid interface. Shown in (a) is the case where the soap film thickness is such that R_1 and R_2 interfere negatively, and an observer would see a dark spot. In (b) the rays interfere constructively to form bright spots. The lower bar shows the brightness variation of the combined reflected rays. (c) is the cylinder wake, revealed by interference, as the soap film flows past the cylinder.

In case the local soap film thickness is h, the additional length traversed by the light ray R_2 is

$$\delta l = 2n_{\mathrm{i}}h\cos\theta + \frac{1}{2}\lambda, \tag{2.4}$$

where n_{i} is the refractive index of the fluid, λ is the wavelength of the light in the liquid solution, and θ is the angle (relative to a surface normal) at which the light reflects inside the soap film. The second term $\frac{1}{2}\lambda$ is due to a 180° phase shift of R_2 as it reflects off the soap film which has a higher refractive index than the air through which it propagates.

Constructive interference, and hence bright spots, are formed between R_1 and R_2 when δl is equal to an integer times the wavelength

$$\delta l = m\lambda, \tag{2.5}$$

as shown in figure 2.4(a). In case the change in thickness results in the rays only be shifted by effectively half a wavelength, i.e.

$$\delta l = \left(\frac{1}{2} + m\right)\lambda, \tag{2.6}$$

interference is destructive and a dark film is seen. The lower bar in figure 2.4 shows the resulting colour from interference of R_1 and R_2 that an observer would see, when the film thickness varies linearly as shown. The change in film thickness from (a) to (b) corresponds to the rays being shifted in phase by half a wavelength.

Let us now consider an incident light ray that meets the soap film along its normal, thus $\cos\theta = 1$. In case the soap film thickness has a slight variation such that two neighbouring points of constructive interference is formed, then $\delta l = 1\lambda$. The associated change in film thickness is, from equation (2.4)

$$\delta h = \frac{\lambda}{4n_{\mathrm{i}}}. \tag{2.7}$$

A good approximation to monochromatic light can be provided by a low-pressure sodium lamp. Its spectrum is narrow and centered around $\lambda = 589.3$ nm (yellow) which is the major part ($\sim 90\%$) of the energy of the visible light emitted by the lamp. For this particular lamp, neighbouring dark or bright areas tell us that the underlying thickness variation in the soap film is $\delta h = 0.11$ μm when the refractive index of water ($n_{\mathrm{i}} = 1.333$) is used. Although the thickness variation is small, it is sufficient for visualising the flow in soap films. A typical example is given in figure 2.4(c) that shows a snapshot of the vortex wake formed behind a stationary cylinder that penetrates perpendicularly the soapfilm as the latter flows steadily downwards.

2.3 Flows in soap films

As mentioned in the introduction it is today fairly common to study two-dimensional flows with soap films and soap film tunnels. Typically, the flow within the film is visualised using thin-film interferometry as described in the previous section. It is important to keep in mind that structures observed in the flow, such as the vortices seen in figure 2.4(c), are in fact thickness variations. It is not the flow itself one sees. A legitimate question arises in this context: How is the thickness field correlated to the velocity field?

The flow within a soap film flows is complicated. It involves internal pressure driven flow, effects of curvature (Young-Laplace pressure), effects of Marangoni- and Gibbs elasticity, dynamics of soap molecules, effects of compressibility (thickness variations of the film), coupling to the flow of the ambient air and motion of waves in the film itself. Chomaz (2001) analysed rigoriously the flow in soap films under the

sole assumption that the flow takes place on a spatial scale L much larger than the film thickness h. L could for example denote the diameter of a vortex $L \sim 0.1$ cm in a soap film of thickness $h \sim 10$ μm. In this typical setting, $h/L \sim 10^{-3}$ which meets the assumption of Chomaz. He then sets up a system of 'master equations' that take into account the effects of Gibbs and Marangoni elasticity, curvature, exchange of soap between the interstitial fluid and the surface, gradients in soap concentration in the bulk, viscous effects due to flow in the soap film plane and viscous effects due to shear stresses at the film surface. He defined a Mach-number equivalent for soap films $M \equiv U/v_{\mathrm{M}}$ and considered the flow in the range $M \ll 1$. In this limit, to leading order, the master system reduces to the two-dimensional Navier-Stokes equation for an incompressible fluid

$$\frac{\partial \boldsymbol{u}}{\partial t} + \boldsymbol{u} \cdot \nabla \boldsymbol{u} = -\nabla \Gamma_{01} + \frac{1}{\mathrm{Re}} \nabla^2 \boldsymbol{u} \tag{2.8}$$

$$\nabla \cdot \boldsymbol{u} = 0. \tag{2.9}$$

where Re is the Reynolds number defined in equation (1.1). Thus, provided that the local flow speed $|\boldsymbol{u}|$ $(= U)$ is small compared with v_{M}, the soap film flow behaves as an incompressible Newtonian fluid where (to leading order) the surface density of soap Γ_{01} plays the role of pressure. An analogy between sound waves in air and Marangoni waves in soap films exists. In air, the finite propagation speed of sound waves is due to compressibility, i.e., molecules being more densely packed in some regions than in other. This gives rise to pressure variations that are of order M_{air}^2. In soap films, the Marangoni waves are driven by 'compressibility' of surface soap molecules, i.e., gradients in concentration of soap on the film surface. These concentration gradients are, like pressure in air, of order M^2 in the limit $M \ll 1$ (Chomaz, 2001). Hence, in this range of M, pressure fluctuations (i.e., fluctuations in Γ_0) can be disregarded.

It is less clear how the thickness field evolves when an underlying flow in the soap film is present. Chomaz & Cathalau (1990) simulated numerically the evolution of the thickness field and found that it follows the vorticity field when the dimensionless parameter $\tau' \sim 10$. τ' is a rough measure of the time it takes soap to migrate to the film surface. It has not been possible to find quantitative numbers for the soap used in this study, so a direct comparison with the results of Chomaz & Cathalau (1990) and Chomaz (2001) is not possible. As we will see in chapter 4, the thickness variations in the soap film correspond beautifully to the vorticity in simulated two-dimensional incompressible Newtonian flows.

In a gravity-driven, vertically flowing soap film tunnel it was deduced from instantaneous measurements of the thickness and vorticity fields that the thickness field follows the flow as a passive scalar (Rivera *et al.*, 1998). By measuring the evolution of quasi two-dimensional turbulence produced behind a comb structure it was found that certain statistics of the flow evolve in accordance with theoretical predictions for incompressible flows. In particular, the observed thickness and vorticity fields appear similar. Interestingly, the thickness and vorticity fields were similar even in situations with fairly large Mach number, $M \sim 0.5$, and relative thickness variations up to 35% were measured. In our experiments we have $M \lesssim 0.4$ which is smaller than in the experiment by Rivera *et al.* (1998). It therefore seems fair to assume that the soap film meets the requirements to behave as predicted by Chomaz (2001).

In conclusion, the important message in this section is stressed: If (parts of) the *observed* thickness field associated with a soap film flow rotates like a vortex, say, we can trust that a rotating vortex indeed *exists* in the two-dimensional flow of the soap film. Furthermore, the flow in the soap film behaves as the flow of a two-dimensional incompressible Newtonian fluid.

2.4 The soap film tunnel

To visualise structures in two-dimensional flows, a soap film tunnel is build. The flow tunnel consists of a vertically flowing thin soap film that is suspended between wires. The design is inspired by the extensive review by Rutgers *et al.* (2001) and it is seen in figure 2.5: An acrylic reservoir is placed atop a rigid metal frame. A precision needle valve is mounted in the bottom of the reservoir, such that the overall flow through the nozzle is directed vertically downwards. Constant pressure head at the valve is maintained by overflowing an acrylic cylinder, 15 cm tall, inside the main reservoir. Two 0.1 cm thick nylon guide wires exit the nozzle in the vertical direction and the guide wires are tightly suspended with a stainless steel weight. The soap film is made by draining a solution of demineralised water and 1.5% soap (Procter & Gamble's Fairy Ultra) from the upper reservior and between the guide wires. When wet, the wires are pulled apart by thin tension-threads at points 60 cm and 125 cm below the nozzle (see figure 2.5), such that they form a section of the constant width 15.2 cm between these points. Above and below these attachment points, the guide wires converge linearly to a single point forming an opening angle of 13.3°.

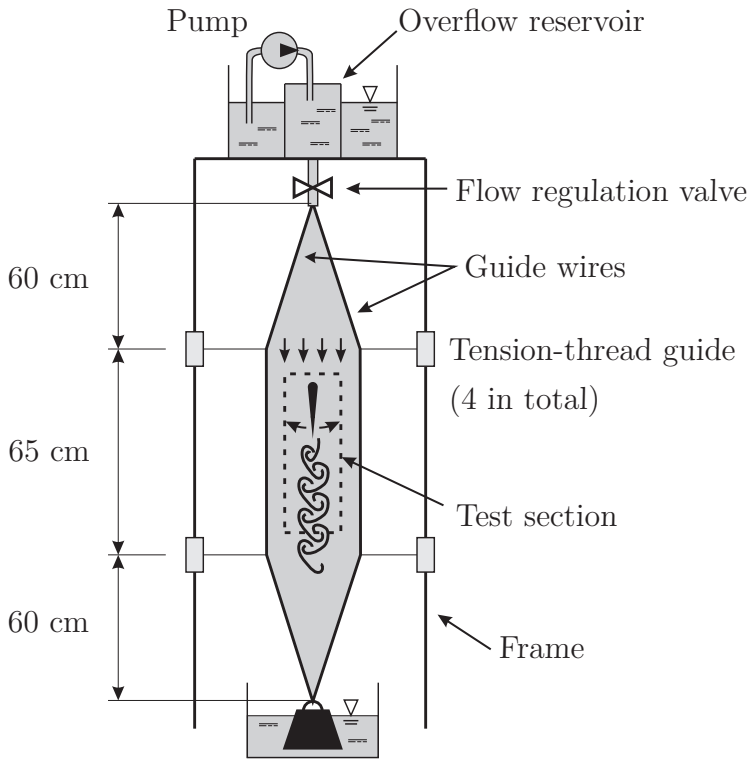

Figure 2.5: Schematic drawing of the gravity-driven soap film tunnel.

The setup is constructed such that the vertical distance between the nozzle and the tension-threads can be continuously varied to optimise the flow tunnel in terms of uniformity, stability and reproducibility. The geometry described above is found be optimal. The thin threads that separate the guide wires are all connected to a single string. In case of an occasional film rupture, the guide wires are brought close together such that the gap is wetted by the draining liquid before pulling them apart to restore the soap tunnel geometry in one easy operation.

The central part of the parallel section, marked by a dotted line in figure 2.5, consitutes the test section. In this part of the soap film, the gravity-driven flow is balanced by drag from the surrounding air. We note that our soap film is wider than what seems to be common ($\sim$ 10 cm) in the literature. It is unclear why this particular value is often used elsewhere, but we found that the wide film better suppresses asymmetric waves and since the tunnel is wider, possible effects from boundaries are less likely to occur.

In the test section the flow is uniform both streamwise and laterally. Free stream flow speeds U can be obtained in the range $110-280$ cm/s by the varying efflux rate through the valve. Typically we operate the tunnel at a velocity of $U = 150$ cm/s. From measurements of the valve efflux rate, film width and flow speed the average

film thickness is found to be $h = 1.5$ μm. By inspecting interference fringes in the test section it is verified that the film thickness is homogeneous to within $\delta h = 0.06$ μm, which yield a 4% uncertainty on the estimated mean film thickness. The free stream flow speed is measured by tracking small air bubbles, pollutants and other defects in the soap film using a high-speed camera. All these identifiable features in the soap film move with speed $U \pm 3\%$, and we take this uncertainty as the uncertainty on flow speed.

The flow structures in the soap film are visualised with thin-film interference as described in section 2.2. We make use of monochromatic light from a low pressure sodium lamp (Philips SOX 90W light bulb) onto the soap film. Monochromatic light has the advantage that it produces interference fringes with high contrast, which makes it easy to identify the flow features. The interference fringes are recorded with a high speed camera (Phantom v4.2 monochrome), and a digital camera (Nikon D70s) with a macro lens (Nikon AF-s VR Micro-Nikkor 105mm f/2.8 IF-ED) for high-resolution pictures. To minimise geometrical distortions of the images, we take care that the incoming rays of light are as perpendicular as possible to the plane of the soap film. Typically, the incident light meet the soap film in an angle of 5.7° off the soap-film normal.

2.5 Effective viscosity of a soap film

Typically, the flow of a Newtonian fluid is characterised by the Reynolds number, in which the fluid viscosity is a key parameter. To compare the flows in the soap film with flows in water or air, we could for instance use a effective soap film viscosity to calculate the Reynolds number for the soap film flow. The (effective) viscosity of soap films is more involved than that of a Newtonian fluid. In fact, it is not even expressed by a single parameter. As shown in figure 2.2, a soap film consists of two surfaces bounding an interstitial fluid. The effective viscosity of the soap film is therefore comprised by viscosity of the interstitial fluid layer, ν_b, and contributions from the two fluid-air interfaces, ν_s. The effective kinematic viscosity is commonly expressed as (Trapeznikov, 1957)

$$\nu_\mathrm{e} = \nu_\mathrm{b} + 2\frac{\nu_\mathrm{s}}{h}. \tag{2.10}$$

For thick films, the bulk contribution dominates, whereas for thin films the terms that account for the surface will dominate. Generally ν_b is taken as the viscosity of

water whereas ν_s depends on the chemical components in the soap.

Several studies have been performed on soap films of varying thicknesses. For example, Martin & Wu (1995) constructed a Couette cell device to measure the viscosity of a freely suspended, horizontal soap film. By rotating a magnet they forced a thin metal annulus to co-rotate as it was suspended in a horizontal soap film (with stationary, circular boundary). From either the transient response of the annulus' angular velocity to a sudden change in the forcing, or from stresses build up in the steadily rotating annulus they inferred the effective viscosity $\nu_e = 0.04$ cm^2/s for films of thickness 0.5 μm $\leq h \leq$ 1μm. Although their experiment is quite fascinating, the method is rather involved and it is hard to precisely control the thickness of the horizontally suspended film.

Gharib & Derango (1989) proposed an alternative method to estimate the viscosity from measurements of vortex shedding frequency, behind cylinders of different diameters. The data, represented by $\mathrm{St_n}$ and Re, can then be fitted to the Strouhal curve determined by Roshko (1954) and mentioned in chapter 1

$$\mathrm{St_n} = 0.212\left(1 - \frac{21.2}{\mathrm{Re}}\right), \qquad \mathrm{Re} < 200 \tag{2.11a}$$

$$\mathrm{St_n} = 0.212\left(1 - \frac{12.7}{\mathrm{Re}}\right), \qquad \mathrm{Re} \geq 200, \tag{2.11b}$$

using the kinematic viscosity as the single fitting parameter. Although Gharib & Derango (1989) did not conduct the actual fitting procedure, the method was adopted by Vorobieff & Ecke (1999a). They considered films of thicknesses in the range 4 μm $\leq h \leq$ 20 μm and found the effective viscosity to vary roughly in the range 3–8 times the viscosity of water. The most viscous film was the thinnest, in agreement with equation (2.10).

The film in our soap film tunnel is fairly thin, $h = 1.5$ μm, and thus it falls outside the range considered by Vorobieff & Ecke (1999a). We therefore adopt their method, and measure the wake frequency f behind 20 different cylinders with diameters varying in the range 0.020 cm $\leq D \leq$ 1.20 cm. The cylinders were placed, one at a time, in the test section of the soap film with free streaming flow speed $U = 150$ cm/s. The cylinders did not oscillate in response to the unsteady fluid-forces. The wake frequency is measured, using high-speed videos, by counting the number (typically ~ 20) of vortices that advect through a fixed reference line in the test section.

In figure 2.6 we show the measurements obtained from the experiment and our

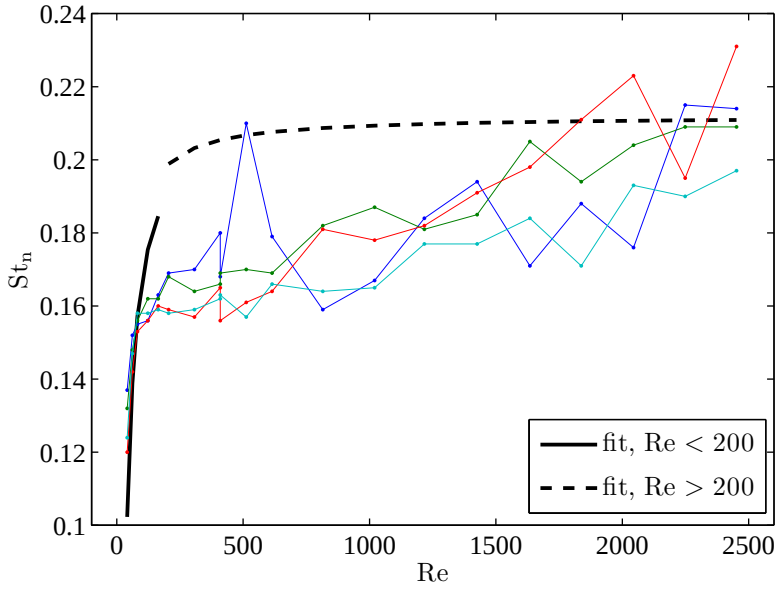

Figure 2.6: Measurement of Strouhal number vs. Reynolds number for circular cylinders in the uniform soap film flow. The curves show the fit of equation (2.11) to the data.

fit of the Strouhal-curve, equation (2.11). The value of ν_e is chosen to minimise the root-mean-square deviation between the mean Strouhal number and (2.11). This gives the estimate $\nu_e = 0.07$ cm^2/s, i.e., under these flow conditions, our soap film has a kinematic viscosity which is approximately seven times the viscosity of water.

It is noted from figure 2.6 that the measured values of $\mathrm{St_n}$ do not seem to be described very well by the $\mathrm{St_n}$-Re curve in equation (2.11). It is not clear to us what causes this discrepancy. The agreement between measurements and the curve (2.11) is better in the study by Gharib & Derango (1989) and Vorobieff & Ecke (1999a). The latter used 15 cylinders with diameters in the range 0.01 cm $\leq D \leq$ 0.26 cm in flows ranging from 90 cm/s $\leq U \leq$ 200 cm/s, which closely matches our experiment. Differences are that our film is thinner and we use the Fairy Ultra detergent, which is likely not used by Vorobieff & Ecke. Couder *et al.* (1989) mention that friction between the soap film and the surrounding air introduces damping and moves the threshold Re at which the vortex shedding takes place. Given that our film is fairly thin it is more subjected to air drag by virtue of the reduced inertia of the soap film. Couder & Basdevant (1986) mention that the formation of a meniscus, a local increase in film thickness, around the cylinder can cause a larger effective diameter of the cylinder. Such a meniscus will therefore result in $\mathrm{St_n}$ being underestimated. No notable meniscus was observed in our experiments, although it was not verified rigorously. An alternative explanation is the wetting ability of the cylinders used.

When the experiments were conducted, the cylinders were not carefully de-greased. In principle, some amount of grease from handling could sit on the cylinders and cause changing wetting properties, which can affect the meniscus. This can explain the large variations in St_n in figure 2.6.

The estimate $\nu_e = 0.07$ cm^2/s still seems fair when it is compared to the value determined by Martin & Wu (1995) and the values determined by Vorobieff & Ecke (1999a). Regardless of the discrepancy between our measured St_n-Re curve and those measured in previous studies we will make use of our estimate $\nu_e = 0.07$ cm^2/s. As we will see in chapter 4, boundary layer flows as well as evolution of vortex wakes match closely between the flows in the soap film and simulated flows of an incompressible two-dimensional Newtonian fluid when the Reynolds number in simulations matches that in the experiments when it is based on the estimated value of ν_e.

2.6 Summary

In this chapter we described the anatomy of soap films, their elastic properties, motions of waves in soap films, and visualisation of thickness variations through thin-film interferometry. Most important, an experimental set-up that makes use of a gravity driven, vertically flowing planar soap film is introduced. An object that penetrates the film modifies the quasi two-dimensional flow. The flow is linked to minute thickness variations that follow the flow as passive tracers, like the dye used to show the flow in a water tunnel. These thickness variations are revealed by thin-film interferometry.

One way to match the soap film flows with simulated flows in water or air, is by using the Reynolds number. This requires an effective viscosity of the soap film tunnel that is estimated, based on a simple experiment, to be $\nu_e = 0.07$ cm^2/s. The estimate is in good agreement with results obtained by other groups.

The soap film tunnel will be used to measure in great detail the periodic vortex wake structures of a rigid foil that flaps at externally controlled frequency and amplitude, presented in the next chapter. Also, in chapter 7 we will make use of a similar soap film tunnel to study interaction of two flappers.

Chapter 3

Vortex wakes of a flapping foil

A swimming creature propels itself with its flapping fin. Fins vary greatly in both size and geometry, some are optimised for speed (like the mackerel) while others are optimised for cruising (like the whale) or maneouverability (like the box fish in figure 1.10). Instead of studying such a specialised foil shape, we will consider the flow of a simple foil. In fact, it is the perhaps simplest realisation of a fin: A rigid foil that performs prescribed pitching oscillation around the leading edge in a two-dimensional flow. In this chapter we consider the wake types behind a rigid, pitching foil.

We show detailed measurements of the vortex wakes behind the pitching foil. The wake types are mapped out in a phase diagram, similar to the Williamson-Roshko map of figure 1.5, spanned by the Strouhal number $0 \leq \mathrm{St}_D \leq 0.3$ and dimensionless amplitude $0 \leq A_D \leq 2$. To measure the wakes we make use of a vertically flowing soap film tunnel as described in the previous chapter. The main advantage of soap film tunnels is the high quality of flow visualisation they provide. Second, the set-up that we use is mechanically very simple and it is easy to operate. Drawbacks are that we cannot, for this system, measure the fluid forces acting on the foil, and the soap film flow is generally complicated. In chapter 4 we will extend the map of vortex wakes with numerically simulated forces, and we will see that the soap film dynamics shows remarkable agreement with the simulated two-dimensional incompressible flow.

We find a phase diagram that is mostly composed of vortex wakes where two vortices are shed per oscillation period. These wakes are either a normal von Kármán wake or an inverted von Kármán wake. In the range $\mathrm{St}_D < 0.1$, wakes with many vortices shed per oscillation period dominate. Simple models are provided to explain (1) the complicated wakes in the low-St_D range, (2) why two distinct and

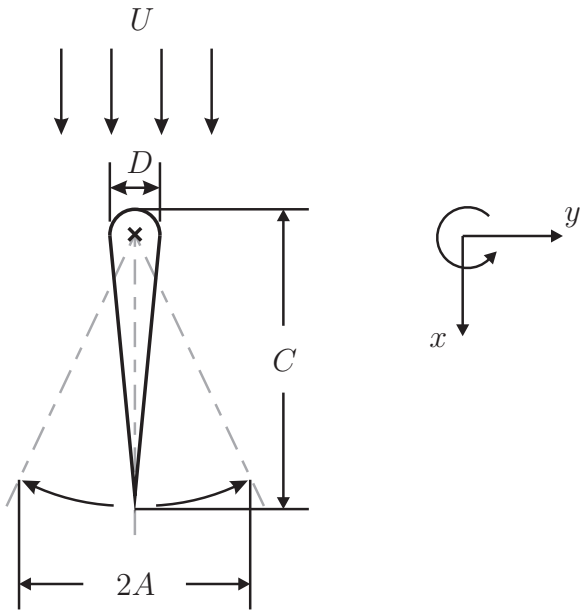

Figure 3.1: Schematic drawing of the foil that performs simple harmonic pitching oscillations around the center of the circular leading edge.

disconnected regions of $2P$ wakes exist and (3) a possible link between constant amplitude based Strouhal number and the boundary between von Kármán and inverted von Kármán wake regions, in terms of vortex strengths.

3.1 Foil geometry and dimensionless numbers

The foil geometry is shown in figure 3.1. The foil has a circular leading edge and straight sides that meet at the sharp trailing edge. The foil is milled out of brass to within an absolute tolerance of 10^{-3} cm. For the experiments two foils are used, one with chord length $C = 0.60$ cm and width $D = 0.10$ cm, and one that is twice this size, i.e., $C = 1.20$ cm and $D = 0.2$ cm.

A two-dimensional flow is provided by the gravity-driven soap film tunnel that was described in section 2.4. In the center of the test-section, cf. figure 2.5, the soap film is penetrated by the foil such that the plane in which the foil pitches is parallel with the soap film. Before each experiment, a layer of oxidised brass is carefully removed with fine sandpaper. Despite its large oscillation frequencies and amplitudes the foil does not lead to film rupture. The foil is attached to a rigid driving shaft that is pitched by an oscillating motor that works as follows: A central shaft is spring loaded such that it experiences a restoring torque when it is rotated away from its resting angle. Permanent magnets attached to the shaft

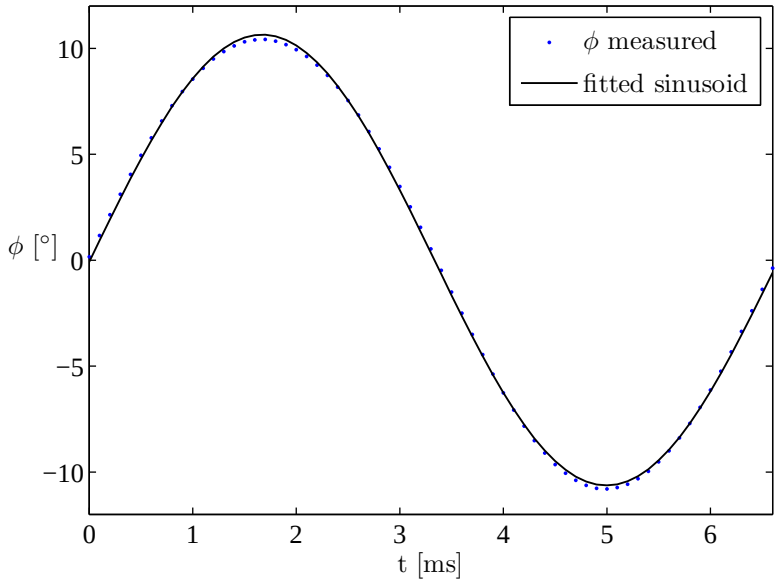

Figure 3.2: Waveform of the pitch angle (relative to vertical) of the foil when it is oscillated at $f = 150$ Hz. The total RMS deviation over one oscillation period is 1.8%.

are displaced with electromagnets such that the axle rotates. When applying an alternating current to the magnets, the shaft performs angular oscillations. The axle is held in position by a rigid teflon cramp. Typically the foil is driven at frequencies in the range 30 Hz $< f <$ 230 Hz at angular amplitudes $\phi_0 \leq 10.5°$. The waveform and angular amplitude of the angular oscillation are monitored by reflecting a laser beam off a mirror that is attached to the shaft and subsequently tracking the beam on a projection screen. A representative waveform of the angular oscillations, the pitching waveform of the foil, is seen in figure 3.2 and the root-mean-square deviation from a pure sinusoid is less than 1.8%. For certain frequencies, the motor oscillates around a mean angle that is different from the resting angle. In such a case, the motor is tilted manually to counteract the bias angle.

Four dimensionless numbers characterise the flapping motion of the pitching foil. As mentioned in the introduction, the pitching oscillation of the foil is expressed by the Strouhal number

$$\mathrm{St}_D = \frac{Df}{U}, \tag{3.1}$$

where f is the prescribed pitching frequency and U is the free stream flow speed. The dimensionless flapping amplitude is

$$A_D = \frac{2A}{D}, \tag{3.2}$$

where $2A$ is the total horizontal excursion of the foil tip, cf. figure 3.1. The foil's aspect ratio

$$\text{A.R.} = \frac{C}{D}, \tag{3.3}$$

is equal to 6 for both foils, and will be keept fixed throughout the thesis.

The last dimensionless number is the Reynolds number based on the free-stream flow speed ($U = 150$ cm/s), foil width ($D = 0.1$ cm or $D = 0.2$ cm) and the effective soap film viscosity determined in section 2.5 ($\nu_\text{e} = 0.07$ cm^2/s)

$$\text{Re} = \frac{DU}{\nu_\text{e}}. \tag{3.4}$$

For the small foil we have Re = 220 and for the large foil we have Re = 440.

A low-pressure sodium lamp provides the monochromatic light to visualise the thickness variations in the soap film, and the flow is effectively monitored in real time with the previewer of a high speed camera. Often, the real-time measurements are supplemented with videos recorded at 2000 frames per second. We scan the space spanned by St_D and A_D in the following way. First, a pitching frequency is selected. Then the amplitude of the pitching oscillations is slowly ramped up until we observe changes in wake structure. Due to the direct monitoring of the flow and the continuously varying A_D it is easy to pinpoint precisely the value of A_D where a wake transition takes place. We find no hysteresis, i.e., no difference in this transition as A_D is increased or decreased.

For the measurements with $\text{St}_D < 0.15$ we make use of the small foil, and for the measurements with $\text{St}_D \geq 0.15$ we make use of the large foil. We presume that for the regime of intermediate Reynolds number, $10^2 < \text{Re} < 10^4$, the wake structures are insensitive to changes in Re since the quasi two-dimensional flow of the soap film is not subject to three-dimensional instabilities. To verify that the wakes measured do not depend on the specific foil size, we scan with the large foil at $\text{St}_D = 0.12$ and with the small foil at $\text{St}_D = 0.18$. These scans show a perfect agreement in the wakes measured for each value of St_D.

3.2 Map of vortex wakes

The measured map of vortex wakes is shown in figure 3.3, using the wake labeling from Williamson & Roshko (1988) in conjunction with a colour coding. The space is spanned by $0 \leq \text{St}_D \leq 0.30$ and $0 \leq A_D \leq 2.0$, and the resolution of the scan

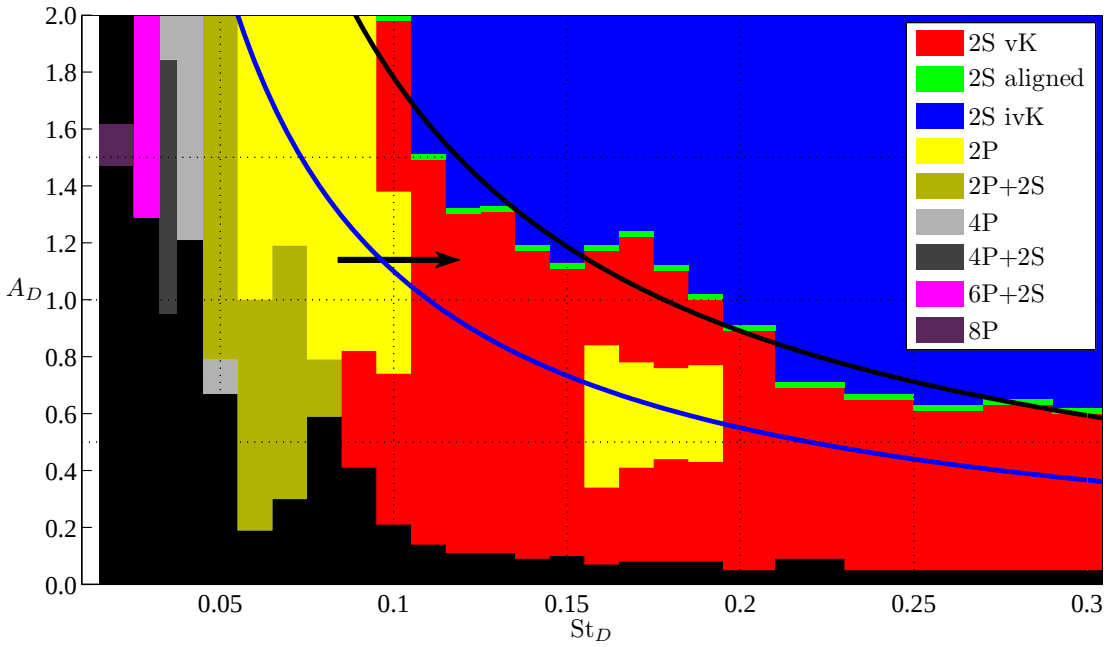

Figure 3.3: Map of vortex wakes in the St_D, A_D plane. The blue line is for $\mathrm{St}_A = 0.11$ and the black line is for $\mathrm{St}_A = 0.18$ (see section 3.4). The figure is reprinted from Schnipper *et al.* (2009).

in frequency is given by the width of the vertical, coloured colums comprising the map.

Several points are worth noting. Firstly, the major part of the map is occupied by wake types that are periodic with the prescribed frequency of the foil. In all observed periodic wakes, an even number of vortices are formed per oscillation period and the wakes are symmetric in the sense that the vortex pattern shed as the foil moves from one extreme position to the other is, except for a change in sign, similar to the pattern shed as the foil moves back. In the range $\mathrm{St}_D \lesssim 0.07$ the wake is extremely sensitive to a slight flapping asymmetry. This sensitivity likely explains the asymmetric wakes (where an odd number of vortices shed per period) measured by Lentink *et al.* (2008). Their driving mechanism, by design, produces an asymmetric oscillation waveform. It is not clear why asymmetric wakes were produced behind the cylinder oscillating transverse to the free flow (Williamson & Roshko, 1988). Behind the rounded cylinder, regions of vorticity (cf. the attached eddies in figure 1.1(a)) interact easier. It is speculated that an asymmetry introduced as the cylinder is started from rest could partly explain the asymmetry. In contrast, the foil's main source of circulation in the low St_D limit is the leading edges. The foil chord functions in this case as an effective wake-splitter that prevents interaction of vorticity formed at the left and right sides of the foil.

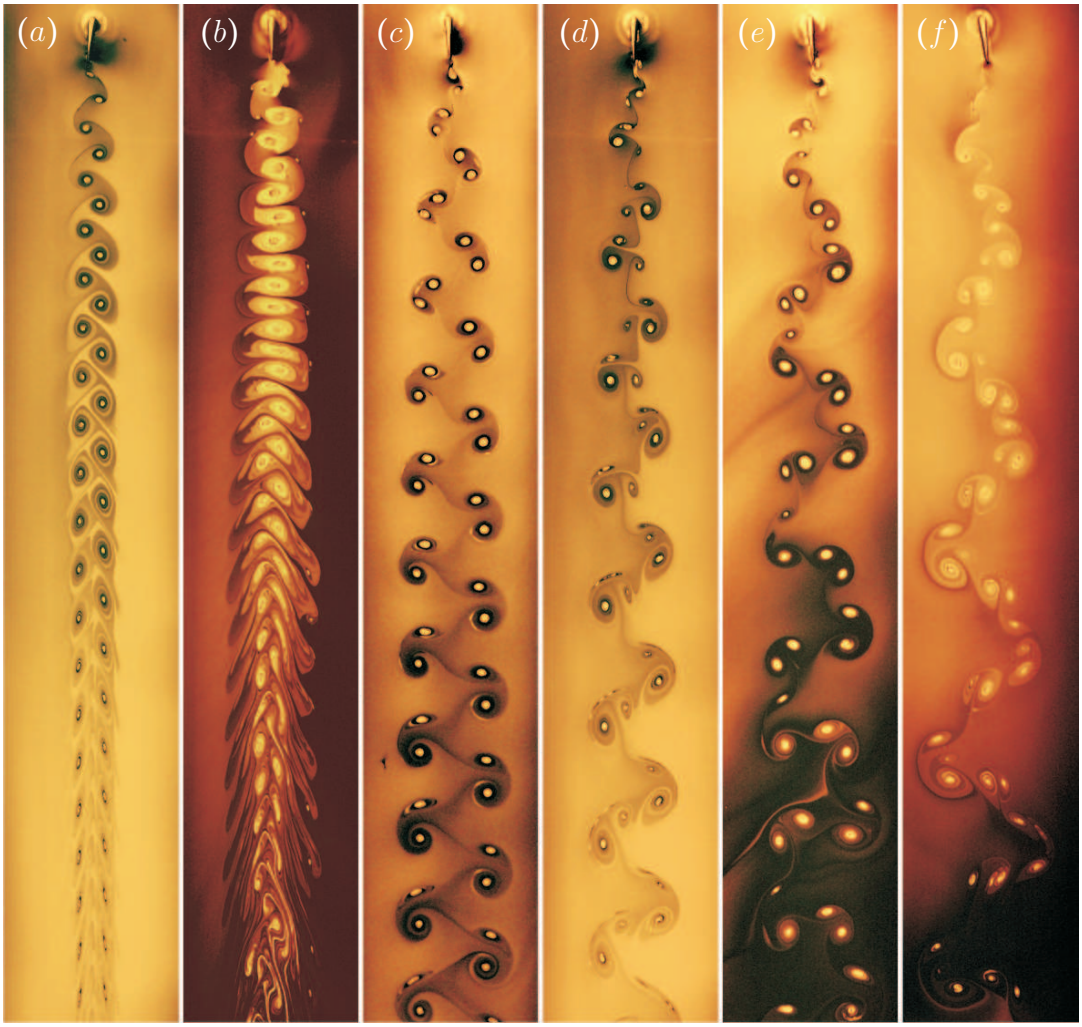

Figure 3.4: Selected wakes types behind the small foil: (a) von Kármán wake for $\mathrm{St}_D = 0.12$ and $A_D = 0.98$, (b) inverted von Kármán wake for $\mathrm{St}_D = 0.12$ and $A_D = 2.0$, (c) $2P$ wake for $\mathrm{St}_D = 0.080$ and $A_D = 1.4$, (d) $2P + 2S$ wake for $\mathrm{St}_D = 0.053$ and $A_D = 1.2$ (e) $4P$ wake for $\mathrm{St}_D = 0.039$ and $A_D = 1.34$ and (f) $4P + 2S$ wake for $\mathrm{St}_D = 0.035$ and $A_D = 1.47$. The figure is reprinted from Schnipper *et al.* (2009).

Asymmetric wakes behind the foil do exist. In the upper-right corner of the map the inverted von Kármán wakes become oblique. This is also found by Godoy-Diana *et al.* (2008) who furthermore show that the asymmetric wake is accompanied by production of an average lift by the foil. In our experiment it is not possible to determine precisely the threshold where the wake becomes oblique. Between the region with von Kármán and inverted von Kármán wakes, we find a wake type where the vortices are aligned, like pearls on a string, behind the foil. As they are advected further downstream the vortices fall back into the usual staggered double-row arrangement of the von Kármán wake.

Secondly, wake types where two vortices are shed per oscillation period, $2S$ wakes, dominate the map—particularly in the region $\mathrm{St}_D > 0.1$. For small A_D, we typically observe von Kármán wakes. Notice how these wakes are found over a wide range of frequencies, as opposed to the case of the stationary cylinder, cf. figure 1.5. As A_D is increased we instead find the inverted von Kármán wake. Examples of these wakes are given in figure 3.4(a, b). Notice that figure 3.4 shows the evolution of the wakes far downstream. Similar visualisations of the far-wake are rare in the literature, the only known example we could find is Zdravkovich (1969) who visualised in one picture 17 periods of the von Kármán wake and Koochesfahani's wake shown in figure 1.8(a). Apart from slow decay of the vortices as they are advected downstream, the von Kármán wake does not change significantly. In contrast, the vortices in the inverted von Kármán wake tear each other apart from around 10 chord lengths downstream. This leaves a blurred wake without clear vortex structures. A similar degeneration of the inverted von Kármán vortex wake is observed behind a NACA-0012 foil oscillating in the purely pitching mode (Koochesfahani, 1989, Fig. 3b) or purely plunging mode (Lai & Platzer, 1999, Fig. 4c) in a water stream.

Thirdly, we observe wake types where two vortex pairs, $2P$, are shed per oscillation period, in agreement with observations behind a pitching airfoil (Koochesfahani, 1986, 1989) and an airfoil oscillating in a pure plunging mode (Lai & Platzer, 1999). An example is given in figure 3.4(c). This wake type is also measured behind live swimming eel (Tytell & Lauder, 2004), in the simulated wake of a swimming eel (Blondeaux *et al.*, 2005), behind bluegill sunfish that perform turning maneouvers (Drucker & Lauder, 2001) and behind the cylinder that oscillates transverse to the free stream (Williamson & Roshko, 1988). In the latter case the wake appeared in a single region in the space spanned by (inverse) frequency and amplitude. For the pitching foil, however, two distinct regions with $2P$ wakes exist: A main region at $\mathrm{St}_D \sim 0.08$, and a little island that is wholly contained in the region with von Kármán wake at $\mathrm{St}_D \sim 0.17$. We will discuss further the $2P$ wake in section 3.3.

Finally, the region with low Strouhal number $\mathrm{St}_D < 0.1$ is dominated by complicated wakes. Shown in figure 3.4(c–f) are examples of such wakes ranging from the $2P$ wake to the complicated $4P + 2S$ wake where 10 vortices form per oscillation period. In general more vortices, up to the impressive 8 pairs, are measured per period as St_D is decreased. For these low values of St_D the wake structure takes the form of a wavy band of vortices. Roughly like a material line, the vortices show the trajectory of the foil tip drawn into the by-passing liquid sheet. Similar measurements were made by Bratt (1953), Koochesfahani (1989) (cf. figure 1.8(a)), and

Lentink *et al.* (2008), although their experiments did not allow the same quantitative observations. That flow structures can be clearly resolved in this low-St_D range shows the visualisation strength of soap film tunnels.

A simple model of the wake in the limit of low St_D can be made following the idea of Ponta & Aref (2005) that was outlined in section 1.2. We consider the shedding frequency of a cylinder with diameter D. The associated Strouhal number for the (natural) vortex shedding in this case is measured as $\mathrm{St}_\mathrm{n} = 0.17$, i.e., the cylinder sheds two vortices during the time

$$T_\mathrm{n} = \frac{D}{U\ \mathrm{St}_\mathrm{n}}. \tag{3.5}$$

Let us now observe the flapping foil over one oscillation period $T = 1/f$, and compare the observation time with $m \cdot T_\mathrm{n}$, where m is an integer. This gives the relation

$$\mathrm{St}_D = \frac{1}{m}\ \mathrm{St}_\mathrm{n}. \tag{3.6}$$

We predict the value of St_D that belongs to a certain wake type, i.e. a certain m, in the table below. For example, $m = 4$ corresponds to a wake type where 8 vortices are shed per oscillation period which corresponds to the $4P$ wake.

m	Wake type	Predicted St_D	Measured St_D
2	$2P$	0.085	~ 0.08
3	$2P + 2S$	0.057	~ 0.05
4	$4P$	0.043	~ 0.04
5	$4P + 2S$	0.034	~ 0.035
6	$6P$	0.028	—
7	$6P + 2S$	0.024	~ 0.03
8	$8P$	0.021	~ 0.02

Table 3.1: Predicted and measured wake types in the low St_D limit.

Given the simplicity of the model, the agreement with measurements is good. The model is only valid in the limit of low St_D, where the wake is comprised of many vortices formed per oscillation period. In this limit, circulation is predominantly produced at the foil's leading edge and vortices form through shear flow instabilities in the wake. This is in agreement with observations in the picture of the $4P + 2S$ wake in figure 3.4(f). Notice here that the first 2 chord lengths downstream of the

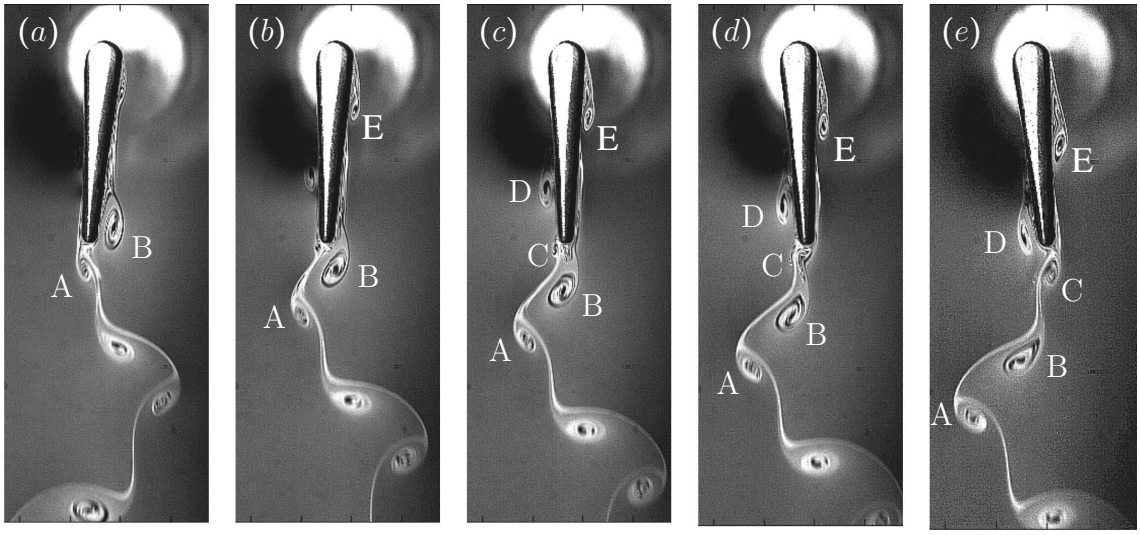

Figure 3.5: Formation of a $2P$ wake ($\mathrm{St}_D = 0.09$ and $A_D = 0.95$). The panels show the foil as it sweeps from the left-most position, panel (a), to the right-most in panel (e). As time progresses, a vortex 'E' is formed close to the leading edge, while another vortex 'C' is formed at the trailing edge as it crosses the vertical line. The figure is reprinted from Schnipper *et al.* (2009).

foil, the wake is blurry. Futher downstream, individual vortices form and become identifiable. The model can not explain the transition from von Kármán to inverted von Kármán wake, where the tip produces significant circulation, nor can it explain the existence of the little $2P$ island. As we shall see in the following sections, timing of vortices shed from the leading and trailing edges explain the $2P$ wake island and the relative strength of leading edge and trailing edge vortices also determines transitions in the wake.

3.3 The $2P$ wake

We will now consider the formation of the $2P$ wake shown in figure 3.4(c). Figure 3.5 shows five zoomed views of the flow around the foil as the tip moves from the left-most position to the right-most.

In figure 3.5(a), two vortical structures are close to the foil tip. Vortex 'A' has a counter clockwise sense of rotation (positive circulation) and it is located immediately under the foil tip. 'B' has a negative sense of rotation and it sits at the lower right side of the foil. As the foil rotates slightly towards the right, panel (b), B is washed into the wake. In the following panels (c–e), A and B are advected into the wake as a vortex dipole on the left side of the center-line. As they move downwards they translate further to the left due to their mutually induced velocity.

Meanwhile in panel (b), separation of the boundary layer close to the leading edge forms an attached leading edge vortex 'E'.

As the foil passes the center-line, panel (c), it achieves its maximal transversal speed and a patch of negative circulation 'C' forms at the trailing edge. In the following panels (d–e), 'D' appears at the tip. D cannot be seen on the preceding panels due to a shadow on the left side of the foil. In panel (e), the foil is in the right-most position and C is shed. Due to symmetry, the half-period of oscillation following panel (e) will be analogous: D will be shed and travel with C as a pair on the right side of the center-line. E will move down along the chord and pair up with the vortex that forms at the tip as it passes the center-line moving leftwards.

Notice how D is created on the left side of the foil, but ends up on the opposite side of the center-line. This is in contrast to the case of a $2P$ wake behind an oscillating cylinder (Williamson & Roshko, 1988). Here, vortices stay on the side of the cylinder where they were formed. $2P$ wakes have also been measured in a horizontal plane that cuts through the center of a swimming eel (Müller *et al.*, 2001). Here it is found that regions of same-signed vorticity, produced at the eel's anterior end, travel down along the body as a 'proto vortex'. The proto vortex follows the undulatory wave that the eel sends down along its spine to swim. When it arrives at the posterior end the protovortex forms, in conjunction with a patch of vorticity produced at the tail, a vortex ring that is shed into the wake. The single vortex ring propagates away from the fish along a path directed only slightly backwards. This wake type is associated with large lift forces (Müller *et al.*, 2001, 2008). Interestingly, the mechanism involved in the formation of $2P$ wake behind swimming eel agree well with the observations done in the soap film tunnel. It therefore seems that deformation of a flexible body is not essential to form a $2P$ wake.

In figure 3.6(a) we show the streamwise position of seven individual leading edge vortices (similar to B, D, E in figure 3.5) as they roll down along the foil chord. The vortices were tracked manually from a high-speed video. It is observed that the vortex centroid moves at an almost constant rate. The red line is a best-line fit to the data points and it has a slope of 72 cm/s, which is close to half the free streaming flow speed of $U = 150$ cm/s. As they move downwards, the leading edge vortices roll, without slipping, as solid wheels downstream along the foil chord. This observation helps to understand the two distinct regions with $2P$ in the wake map in the following simple way: The time it takes a detached leading edge vortex to

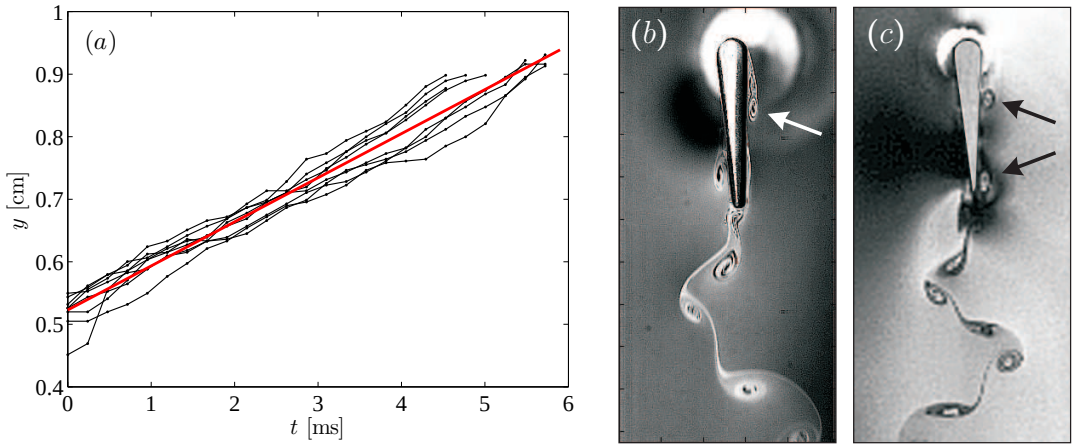

Figure 3.6: (a) Measured position of the leading edge vortices as they roll down along the chord in figure 3.6 (a). The straight red line is fitted to the data. A $2P$ wake in the main region (b), and in the little $2P$ island, (c). Note that in (c), two vortices roll down as a little train (marked with black arrows) along the foil chord. In (b), only one such vortex exists (marked with a white arrow).

advect with speed $U/2$ along the chord C is

$$T_{\mathrm{a}} = \frac{2C}{U}. \tag{3.7}$$

Provided the advection time equals an integer, n, times the oscillation period T, wakes of the $2P$ type can exist. With the foil geometry $C = 6D$ we predict $2P$ wakes when

$$\mathrm{St}_D = \frac{n}{12}. \tag{3.8}$$

For $n = 1$ we predict $\mathrm{St}_D = 0.083$ in excellent agreement witht the wake map. This is analogous to the situation where one vortex is present on each side of the foil chord, as shown again in figure 3.6(b). When $n = 2$ we predict $\mathrm{St}_D = 0.17$, again in good agreement with the wake map. In this case, two vortices must exist simultaneously on each side of the chord which is shown with arrows in figure 3.6(c) (only the flow on the foil's right side is visible in the figure). In principle, the model predicts more islands with $2P$ wakes. However, viscous effects prevents formation of $2P$ wakes at, say, $\mathrm{St}_D = 0.25$ and beyond. Here, the vortices are shed too close to each other in the streamwise direction whereupon they instantly merge two-by-two leaving a wake of $2S$ type.

The simple model helps to understand the existence and location of regions of $2P$ wakes in the wake map. Understanding the boundary between the regions with

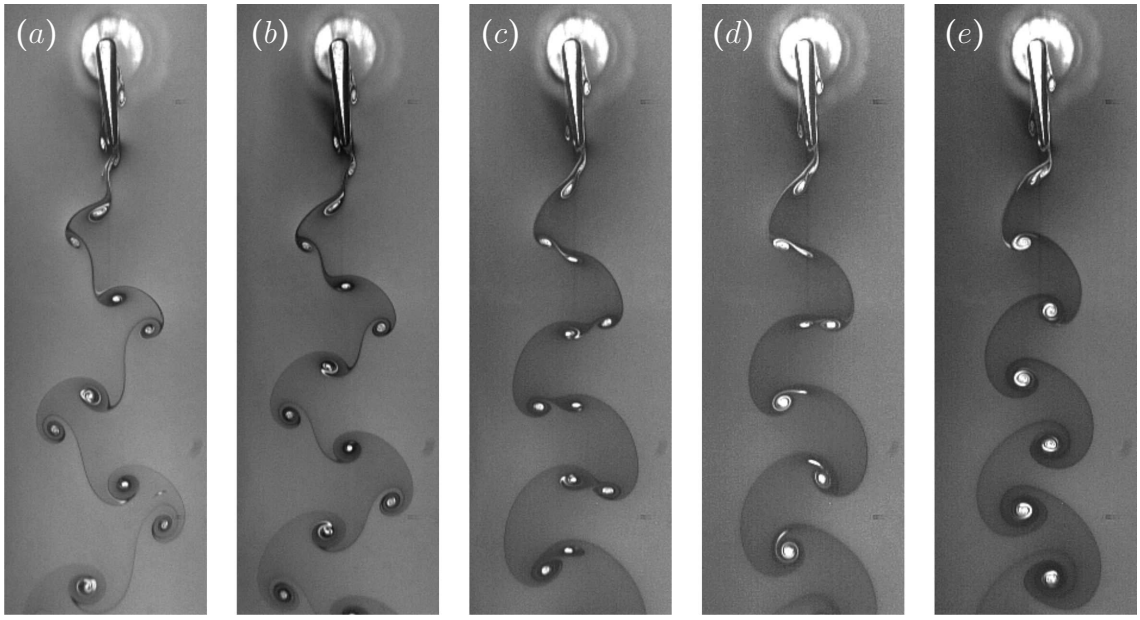

Figure 3.7: Wake types observed following the horizontal arrow in the wake map, figure 3.3, with constant flapping amplitude $A_D = 1.14$. (a) is well within the main $2P$ wake region of the wake map, and (e) is well within the von Kármán wake region. (a) $\mathrm{St}_D = 0.084$, (b) $\mathrm{St}_D = 0.096$, (c) $\mathrm{St}_D = 0.105$, (d) $\mathrm{St}_D = 0.109$ and (e) $\mathrm{St}_D = 0.12$. The figure is reprinted from Schnipper *et al.* (2009).

$2P$ wakes and, say, von Kármán wakes is more involved. To predict the extent of the $2P$ wake island, a criteria for merging of vortices, given their relative position and strength is needed. Notice that the left and right boundaries can be determined by the timing at which the vortices are shed only. The upper and lower boundaries, on the other hand, should be predicted by taking into account the strength ratio. This will be considered in the next section.

3.4 Wake transitions

The formation of a $2P$ wake requires that the timing criteria in equation (3.8) is met. In figure 3.7 we show five snapshots of the flow around the foil as the flapping frequency is increased as shown by the horizontal arrow in figure 3.3. Panel (a) is for the lowest value of St_D and panel (e) is for the highest value of St_D. The individual panels show the foil as it is pitched approximately to the right-most position.

Panel (a) shows a $2P$ wake at $A_D = 1.14$ and $\mathrm{St}_D = 0.84$, i.e., parameters well within the main $2P$ region in the wake map. As the flapping frequency is increased, the leading and trailing edge vortices are shed with a still smaller streamwise sep-

aration, a good example is the wake change from panel (b) to panel (c). In this situation the trailing edge vortex is shed close to the same-signed leading edge vortex from the preceeding oscillation half-period. As the wake evolves, the trailing edge vortex induces a large strain on the same-signed leading edge vortex, and ultimately they merge further downstream (not shown in c). In panel (d), the merging of same-signed vortices occurs approximately one chord length downstream of the trailing edge. Upon the slight increase in St_D, from $\mathrm{St}_D = 0.11$ in (d) to $\mathrm{St}_D = 0.12$ in (e), one cannot distinguish in the wake between patches of vorticity formed at the leading and trailing edges. In this panel, the vortices leave the trailing edge simultaneously.

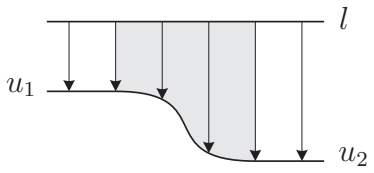

From the experimental observations it is clear that essentially two sources of circulation exist: The leading edge and the trailing edge. In total the two edges form four patches of vorticity per oscillation period. We model the strength of these patches by following the idea of Prandtl & Tietjens (1934). Consider the transport of circulation through the one-dimensional area of the straight line l, as shown on the sketch to the right. Vorticity only exists in regions where the velocity has a non-zero gradient, i.e., circulation flows in the shaded area only. The rate at which circulation flows through l is,

$$\frac{\mathrm{d}\Gamma}{\mathrm{d}t} = \frac{u_2^2 - u_1^2}{2}, \tag{3.9}$$

where u_1, u_2 are the components of velocity normal to l. Let us consider the vorticity that flows past a line that extends horizontally to the right, starting at the foil's round leading edge. Observations show that a leading edge vortex is formed on sides of the foil during one oscillation period cf. figure 3.5. We assuming that the circulation flowing through l is all collected in a single patch of vorticity, and we estimate the circulation of this patch as

$$\Gamma_{\mathrm{le}} = \frac{1}{2}\int_0^{1/f} U^2 \,\mathrm{d}t = \frac{U^2}{2f} = DU\frac{1}{2\mathrm{St}_D}, \tag{3.10}$$

using $u_1 = 0$ due to the no-slip condition and $u_2 = U$. In the estimate we neglected contributions due to the foil's rotation (this effect is of order $\sim 0.3\%$). Notice that equation (3.10) differs by a factor 2 from the expression given in Schnipper *et al.* (2009). The latter was integrated over a wrong period of time.

At the trailing edge we make use of the same idea, however we apply it in

a situation where the free streaming flow is neglected. The amount of vorticity transported across the trailing edge due to its motion is estimated as

$$\begin{aligned} \Gamma_{\mathrm{te}} &\approx \frac{1}{2}\int_0^{1/2f} [V_{\mathrm{te}}(t)]^2 \ \mathrm{d}t \\ &\approx \frac{1}{2}\pi^2 A^2 f = DU\frac{1}{8}\pi^2 A_D^2 \mathrm{St}_D, \end{aligned} \tag{3.11}$$

where $V_{\mathrm{te}}(t)$ is the instantaneous speed of the foil tip. We presume that equation (3.10) estimates the circulation of the leading edge vortices well, and that equation (3.11) underestimates the circulation produced since the free streaming flow is neglected.

Taking the ratio between Γ_{te} and Γ_{le} yields an expression for the relative strength of the two vortices formed at the leading and trailing edges, i.e.,

$$\frac{\Gamma_{\mathrm{te}}}{\Gamma_{\mathrm{le}}} \approx \frac{1}{4}\pi^2 \mathrm{St}_A^2, \tag{3.12}$$

where St_A $(= \mathrm{St}_D \cdot A_D)$ is the amplitude-based Strouhal number.

In the wake map, figure 3.3, we have included two lines of constant St_A. The blue line is for $\mathrm{St}_A = 0.11$ and the black line is for $\mathrm{St}_A = 0.18$. Notice how the blue line nicely penetrates the regions with $2P$ wakes, and how the points with aligned $2S$ wake follow the trend of the line of $\mathrm{St}_A = 0.18$. These obervations suggest that in the range $\mathrm{St}_D \gtrsim 0.1$, changes in wake structure such as the transition from von Kármán wake to inverted von Kármán wake is linked to the ratio of circulation produced at the leading and trailing edges which is described by St_A^2. For the $2P$ wake we have that the strength ratio of the vortices in a pair is constant along $\mathrm{St}_A = 0.11$. However as we slide along the contour, the relative position of the vortices change, which in some cases lead to merging of vortices as shown. As we shall se in the next chapter, St_A is an important parameter that also describe changes in the average streamwise force on the foil.

3.5 Summary and discussion

This chapter concerned the vortex wakes of a pitching foil in a two-dimensional flow. Using a soap film tunnel we measured a rich variety of periodic and symmetric vortex wakes and presented these in a 'wake map' spanned by the dimensionless flapping frequency, the Strouhal number St_D, and the dimensionless flapping amplitude A_D.

When the foil flaps at $\mathrm{St}_D < 0.1$, a complicated wake is formed where several (up to sixteen) vortices are formed each oscillation period. Flapping in this range, the sharp trailing edge adds only little to the circulation going into the wake. The circulation is mostly produced at the foil's leading edge, and it is subsequently distributed into the wake by the periodic motion of the foil. Once in the wake, shear flow instabilities cause roll-up of vortices a few chord lengths downstream. In the case of $2P$ wake, the individual wake vortices were shown to form at the leading edge and at the trailing edge.

In the range $0.1 < \mathrm{St}_D < 0.3$ and small flapping amplitudes $A_D \sim 0.6$, we see how patches of circulation produced at the foil's leading edge and trailing edge in some cases merge to form a classical von Kármán wake. In other cases, a patch is shed such that it persists as a single vortex in the $2P$ wake. An interesting observation is the existence of a little '$2P$ wake island' surrounded by a sea of von Kármán wakes. A necessary condition for the formation of a $2P$ wake is that vortices formed at the leading and trailing edge are shed sufficiently far apart in the downstream direction. The relative magnitude of circulation produced at the leading and trailing edge is shown to be described by the amplitude-based Strouhal number St_A. These circulations are each taken as the strength of leading and trailing edge vortices. The far-wake evolution of the $2P$ wake indicate that the vortices comprising a pair are of almost equal strength. It therefore seems reasonable that the two regions of $2P$ wake are well penetrated by lines of constant St_A. For larger flapping amplitude, the von Kármán wake transists to the inverted von Kármán wake which is often measured behind swimming fish and taken as an indicator of thrust production. In an intermediate state, the vortices are aligned on the center-line of the set-up. The transition from von Kármán wake to inverted von Kármán wake is also well described by the line $\mathrm{St}_A = 0.18$.

It should be noted that the soap film allows measurements of the wake evolutions in the far-wake, which is attractive for comparison with theoretical models of periodic point vortex wakes. At Virginia Tech, Mark Stremler and co-workers have analysed figure 3.4(c) and compared it with a point vortex model (Salmanzadeh & Stremler, 2009). In this model the wake is assumed infinitely long, i.e., there is no foil. The periodic wake considered is the periodic juxtaposition of a 'block' that is occupied by four vortices. The vortices have equal magnitude, two of which are positive and two are negative. Imposing symmetry arguments on the vortex dynamics, their analysis gives three regimes of qualitatively different wake evolution. The $2P$ wake of figure 3.4 evolve according to the point vortex model's 'scatter' regime, where

vortex dipoles are formed and subsequentently shoot away from the center line. A very recent generalisation of the point vortex model, to be presented (Basu *et al.*, 2010), allows for unequal vortex strengths.

A drawback of the present set-up is the lacking ability to measure directly the fluid forces. The metal axle to which the foil is attached was held in station by a teflon cramp which prevents deflections of the axle. Force measurements using strain-gauges are therefore not possible. Even if such deflection allowed, the tiny fluid forces on the foil yield a tiny deflection of the axle. For example, taking the typical drag acting on a flapper (6 dynes, see chapter 7) as an estimate of the force variation on the foil, the displacement of the axle end is $\sim 10^{-6}$ cm. Even if such displacements could be measured, vibrations of the setup should be accounted for. As we shall see in chapter 7, it is in some cases possible to measure (average) fluid forces in a soap film.

We believe that our results carry important messages for the field of unsteady aerodynamics. Formation of vortices at the foil leading edge is of fundamental importance as they often yield large transient fluid forces on the foil (Dickinson *et al.*, 1999; Sørensen & Nygreen, 2001). For the cylinder oscillating transverse to the flow, vortex formation close to the cylinder gives rise to unsteady fluid forces. Selected changes in oscillation frequency or amplitude, leads to abrupt changes in the lift and drag, which again is reflected by changes in the wake structure.

It is natural to ask if similar transient forces or sensitive dependence on the flapping parameters occur for the pitching wing. This is considered in the next chapter, where we will extend the vortex wakes measured in the soap film tunnel with wakes and fluid forces obtained numerically.

Chapter 4

Unsteady fluid forces

Currently unavailable

Chapter 5

Japanese fan flow

In the previous chapters we considered a foil that imprints a wake in the open flow to which the foil is presented. In this chapter we consider the alternative situation: What is the flow due to a foil that is pitching in an otherwise quiescent flow? In this case there is no free-stream to carry away the vortices formed at the foil. The situation mimics the well-known experience as we create a cooling breeze by flapping a paper-fan, like those used by the Japanese Geishas, or the footprint of a fish that suddently sets into motion from standstill.

5.1 Experimental set-up

A horizontal soap film suspended in a circular loop of metal wire ($\varnothing$ 10 cm) consitutes the flow area. The soap solution used so far in this dissertation do not provide a sufficiently long-lived, stable soap film. Instead the Sterling Johnson big-bubble recipe is used. It consists of demineralised water, 5% Fairy Ultra detergent, 5% glycerin, 0.16% hydroxyethyl cellulose, 1.0% lauramidopropyl betaine, 0.80% propylene glucol, and 0.20% peg-80 sorbitan laurate. This solution produces soap films that are stable for ~ 1 minute.

We make use of the motor presented in chapter 3 to flap the large foil (1.2 cm chord and 0.2 cm diameter) in the soap film. The foil penetrates the soap film from below and flaps in the plane of the soap film. The foil performs simple harmonic pitching oscillations at 100 Hz and a lateral tip excursion $2A = 0.15$ cm. Based on the tip-speed of the foil, the foil diameter and the kinematic viscosity determined in section 2.5, the Reynolds number is of order ~ 130.

Images are aquired with a digital camera (Nikon D70 with macro lens Nikon AF-s VR Micro-Nikkor 105mm f/2.8 IF-ED), operated at shutter speed 1/100 s and

aperture f/10. The camera sees the reflected image of a stroboscopic lamp that is directed towards the plane of the soap film at an angle $\sim 10^\circ$ off the soap film normal. The stroboscopic lamp emits short flashes at the same frequency as the oscillating foil.

5.2 The Japanese fan flow

Figure 5.1 shows the flow caused by the pitching foil. In contrast to the situation in the previous chapters, there is no imposed free streaming flow to produce circulation at the foil's leading edge—it is predominantly the sharp trailing edge that can manipulate the fluid. As the foil tip moves from one extreme position to the other, a lobe of circulating fluid is formed. In the figure, the foil has just moved to the left whereby the lobe with a counter-closkwise sense of rotation is formed. At the counter stroke, a lobe with the opposite sense of rotation will form. In the initial strokes, the fanning flow is limited to a small area near the tip, approximately a size set by the flapping amplitude, and as time evolves the area affected by the tip grows. We tested effect of walls by performing experiments in a circular frame ($\varnothing$ 15 cm) and a quadratic frame with side length 15 cm. No effect of the frame size or geometry are observed.

The lobes are successively advected downwards, thereby creating a streaming flow which is seen in the stripes on each side of the tip. While the lobes are being advected downwards, they undergo severe deformations. In the streamwise direction they are compressed while in the lateral direction they are stretched. A secondary flow folds the layered pattern upwards, thereby forming two regions of slowly rotating fluid. This secondary folding gives the overall flow a beautiful butterfly-like structure. The butterfly wings rotate like a vortex dipole where flow is downwards near the tip. Both the formation of vortical lobes at the foil tip and the formation of large circulating regions due to the secondary flow agree with observations of the flow due to a cantilever plate that is vibrated at the clamped end at Reynolds number $\mathrm{Re} \sim 100$ (Kim & Wereley, 2004).

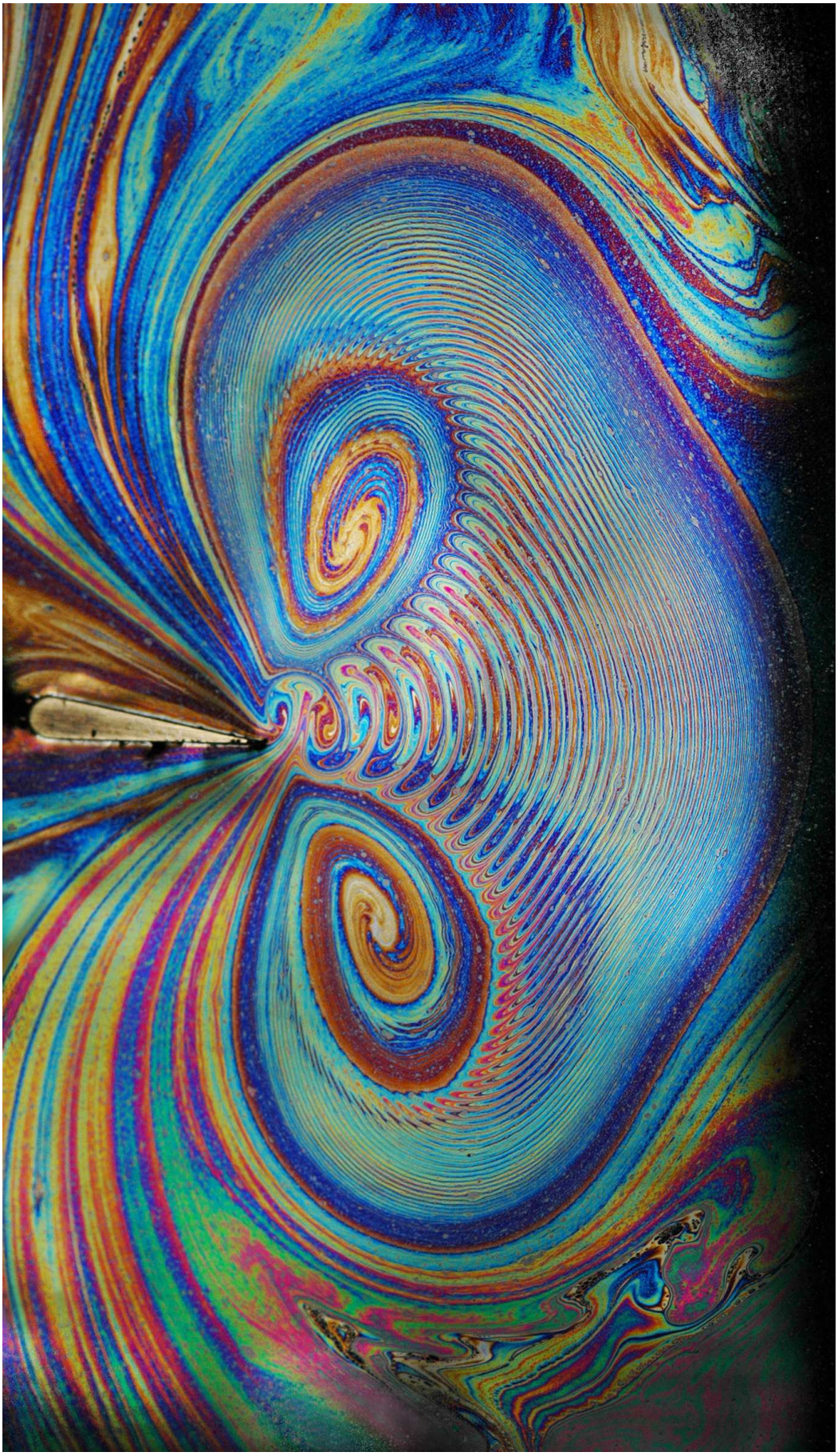

Figure 5.1: The flow of a hand-held paper fan is mimicked by the rapidly pitching foil in a horizontal and otherwise quiescent soap film.

5.3 Discussion

The overall features of the fanning flow agree with observations of the flow of air due to a vibrating cantilever plate (Kim & Wereley, 2004). The plate (3.3 cm long, 3.8 cm wide and 0.013 cm thick) is clamped in one end while the base is oscillated perpendicular to the otherwise free plate. Based on oscillation frequency 180 Hz, tip velocity and amplitude their Reynolds number varied in the range 43–146. Kim & Wereley (2004) reveal the phase-resolved and mean flow fields with micro PIV. In agreement with observations in the soap film, they find that vortices form at the plate's free end. Two vortices form each oscillation period, each vortex formed as the plate moves from one extreme position to the other. Close to the tip the flow is almost two-dimensional, but shortly after being shed the vortices disintegrated due to three-dimensional effects.

A remarkable feature of figure 5.1 is the long history contained in the thickness variations that give rise to the colourful pattern. Take a look at the side of the stacked lobes and follow it all the way to the very center of the wings. Here, the traces of the very first oscillation periods persist—even after ~ 70 oscillation periods! We speculate that non-Newtonian effects are at play in the formation of the flow pattern, and possibly in the long history contained in the picture.

The picture was one of five winning entries in the 2009 Gallery of Fluid Motion poster contest (American Physical Society, 62nd Division of Fluid Dynamics meeting). Also, it has been displayed in the major Danish newspaper "Weekendavisen" (January 22nd 2010) and the homepages of National Geographics and Discovery Channel.

Chapter 6

Free swimming of a pitching foil

Currently unavailable

Chapter 7

Interaction of tandem flappers

Currently unavailable

Chapter 8

Discussion and outlook

Currently unavailable

Bibliography

Anderson, J. M., Streitlien, K., Barrett, D. S., & Triantafyllou, M. S. (1998). *Oscillating foils of high propulsive efficiency.* Phys. Rev. Lett. **360**, 41–72.

Basu, S., Stremler, M., Schnipper, T., & Andersen, A. (2010). *Mathematical modeling of "2P" mode vortex wakes.* 63rd Annual Meeting of the APS Division of Fluid Dynamics. Contributed talk GN.00003.

Batchelor, G. K. (1967). *An introduction to fluid dynamics.* Cambridge University Press.

Blake, R. W. (1981). *Mechanics of ostraciiform propulsion.* Can. J. Zool. **59**, 1067–1071.

Blondeaux, P., Fomarelli, F., & Guglielmini, L. (2005). *Numerical experiments on flapping foils mimicking fish-like locomotion.* Phys. Fluids **17**, 113601.

Bohl, D. G., & Koochesfahani, M. M. (2009). *MTV measurements of the vortical field in the wake of an airfoil oscillating at high reduced frequency.* J. Fluid Mech. **620**, 63–88.

Boys, C. V. (1890). *Soap bubbles - their colors and forces which mold them.* (Reprint) Dover Publications, N.Y., USA.

Bratt, J. B. (1953). *Flow patterns in the wake of an oscillating aerofoil.* Aeronautical Research Council, R & M **2773**, 1–28.

Brøns, M., Jakobsen, B., Niss, K., Bisgaard, A. V., & Voigt, L. K. (2007). *Streamline topology in the near wake of a circular cylinder at moderate reynolds numbers.* J. Fluid Mech. **584**, 23–43.

Buchholz, J. H. J., & Smits, A. J. (2008). *The wake structure and thrust performance of a rigid low-aspect-rato pitching panel.* J. Fluid Mech. **603**, 331–365.

Chomaz, J. M. (2001). *The dynamics of a viscous soap film with soluble surfactant.* J. Fluid Mech. **442**, 387–409.

Chomaz, J. M., & Cathalau, B. (1990). *Soap films as two-dimensional classical fluids.* Phys. Rev. A **41**, 2243–2245.

Couder, Y., & Basdevant, C. (1986). *Experimental and numerical study of vortex couples in two-dimensional flows.* J. Fluid Mech. **173**, 225–251.

Couder, Y., Chomaz, J. M., & Rabaud, M. (1989). *On the hydrodynamics of soap films.* Physica D **37**, 384–405.

Dewar, J. (1923). *Soap films as detectors: Stream lines and sound.* Proc. Roy. Inst. **24**, 197–259.

Dewar, J. (1927). *Collected papers by Sir James Dewar. In:* — ed. by Lady Dewar, with assistance of J. D. Hamilton Dickson, H. Munro Ross, and E. C. Scott Dickson. Cambridge University Press.

Dickinson, M. H., Lehmann, F.-O., & Sane, S. P. (1999). *Wing rotation and the aerodynamic basis of insect flight.* Science **284**, 1954–1960.

Drucker, E. G., & Lauder, G. V. (1999). *Locomotor forces on a swimming fish: Three-dimensional vortex wake dynamics quantified using digital particle image velocimetry.* J. Exp. Biol. **202**, 2393–2412.

Drucker, E. G., & Lauder, G. V. (2001). *Wake dynamics and fluid forces of turning maneuvers in sunfish.* J. Exp. Biol. **204**, 431–442.

Ellenrieder, K. D. von, Parker, K., & Soria, J. (2003). *Flow structures behind a heaving and pitching finite-span wing.* J. Fluid Mech. **490**, 129–138.

Garrick, I. E. (1936). *Propulsion of a flapping and oscillating airfoil.* NACA report **567**, 1–9.

Gharib, M., & Derango, P. (1989). *A liquid film (soap film) tunnel to study two-dimensional laminar and turbulent shear flows.* Physica D **37**, 406–416.

Godoy-Diana, R., Aider, J.-L., & Wesfreid, J. E. (2008). *Transitions in the wake of a flapping foil.* Phys. Rev. E **77**, 016308.

Henderson, R.D. (1997). *Nonlinear dynamics and pattern formation in turbulent wake transition.* J. Fluid Mech. **352**, 65–112.

Hove, J. R., O'Bryan, L. M., Gordon, M. S., Webb, P. W., & Weihs, D. (2001). *Boxfishes (Teleostei: Ostraciidae) as a model system for fishes swimming with many fins: Kinematics.* J. Exp. Biol. **204**, 1459–1471.

Hu, D. L., Chan, B., & Bush, J. W. M. (2003). *The hydrodynamics of water strider locomotion.* Nature **424**, 663–666.

Isenberg, C. (1992). *The science of soap films and soap bubbles.* Dover Publications, Mineola, N.Y., USA.

Jia, L.-B., & Yin, X.-Z. (2009). *Response modes of a flexible filament in the wake of a cylinder in a flowing soap film.* Phys. Fluids **21**, 101704.

Kellay, H., Wu, X.-L., & Goldburg, W. I. (1995). *Experiments with turbulent soap films.* Phys. Rev. Lett. **74**, 3975–3978.

Kim, Y.-H., & Wereley, S. T. (2004). *Phase-resolved flow fields produced by a vibrating cantilever plate between two end plates.* Phys. Fluids **16**, 145–162.

Koochesfahani, M. M. (1986). *Wake of an oscillating airfoil.* Phys. Fluids **29**, 2776. Gallery of Fluid Motion.

Koochesfahani, M. M. (1989). *Vortical patterns in the wake of an oscillating airfoil.* AIAA J. **27**, 1200–1205.

Lai, J. C. S., & Platzer, M. F. (1999). *Jet characteristics of a plunging airfoil.* AIAA J. **37**, 1529–1537.

Lentink, D., Muijres, F. T., Donker-Duyvis, F. J., & van Leeuwen, J. L. (2008). *Vortex-wake interactions of a flapping foil that models animal swimming and flight.* J. Exp. Biol. **211**, 267–273.

Liao, J. C., Beal, D. N., Lauder, G. V., & Triantafyllou, M. S. (2003). *Fish exploiting vortices decrease muscle activity.* Science **302**, 1566–1569.

Lucassen, J., van den Tempel, M., Vrij, A., & Hesselink, F. Th. (1970). *Waves in thin liquid films. 1. Different modes of vibration.* Proc. K. Ned. Akad. Wetensch. B **73**, 109–123.

Martin, B., & Wu, X. L. (1995). *Shear flow in a two-dimensional couette cell: A technique for measuring the viscosity of free-standing liquid films.* Rev. Sci. Instr. **66**, 5603–5608.

Morse, T. L., & Williamson, C. H. K. (2009). *Prediction of vortex-induced vibration response by employing controlled motion.* J. Fluid Mech. **634**, 5–39.

Müller, U. K., van den Heuvel, B. L. E., Stamhuis, E. J., & Videler, J. J. (1997). *Fish foot prints: Morphology and energetics of the wake behind a continuously swimming mullet (chelon labrosus risso).* J. Exp. Biol. **200**, 2893–2906.

Müller, U. K., Smit, J., Stamhuis, E. J., & Videler, J. J. (2001). *How the body contributes to the wake in undulatory fish swimming: Flow fields of a swimming eel (anguilla anguilla).* J. Exp. Biol. **204**, 2751–2762.

Müller, U. K., van den Boogaart, J. G. M., & van Leeuwen, J. L. (2008). *Flow patterns of larval fish: Undulatory swimming in the intermediate flow regime.* J. Exp. Biol. **211**, 196–205.

Patridge, B. L., Pitcher, T., Cullen, J. M., & Wilson, J. (1980). *The three-dimensional structure of fish schools.* Behav. Ecol. Sociobiol. **6**, 277–288.

Ponta, F. L., & Aref, H. (2004). *Strouhal-Reynolds number relationship for vortex streets.* Phys. Rev. Lett. **93**, 084501.

Ponta, F. L., & Aref, H. (2005). *Vortex synchronization regions in shedding from an oscillating cylinder.* Phys. Fluids **17**, 011703.

Prandtl, L., & Tietjens, O. G. (1934). *Fundamentals of hydro- and aeromechanics.* Dover Scientific.

Ristroph, L., & Zhang, J. (2008). *Anomalous hydrodynamic drafting of interacting flapping flags.* Phys. Rev. Lett. **101**, 194502.

Rivera, M., Vorobieff, P., & Ecke, R. E. (1998). *Turbulence in flowing soap films: Velocity, vorticity, and thickness fields.* Phys. Rev. Lett. **81**, 1417–1420.

Roshko, A. (1954). *On the development of turbulent wakes from vortex streets.* NACA rep. 1191.

Rutgers, M. A. (1998). *Forced 2d turbulence: Experimental evidence of simultaneous inverse energy and forward enstrophy cascades.* Phys. Rev. Lett. **81**, 2244–2247.

Rutgers, M. A., Wu, X. L., & Daniel, W. B. (2001). *Conducting fluid dynamics experiments with vertically falling soap films.* Rev. Sci. Instr. **72**, 3025–3037.

Salmanzadeh, A., & Stremler, M. (2009). *A mathematical model of a "2P mode" vortex wake.* Contributed talk BT.00003.

Sasaki, K., Suzuki, N., & Saito, H. (2010). *Bénard-von Kármán vortex street in a Bose-Einstein condensate.* Phys. Rev. Lett. **104**, 150404.

Schnipper, T., Andersen, A., & Bohr, T. (2009). *Vortex wakes of a flapping foil.* J. Fluid Mech. **633**, 411–423.

Sørensen, J. N., & Nygreen, P. J. (2001). *Unsteady vorticity-streamfunction algorithm for external flows.* Computers & Fluids **30**, 69–87.

Taneda, S. (1956). *Experimental investigation of the wakes behind cylinders and plates at low reynolds numbers.* J. Phys. Soc. Japan **11**, 302–307.

Taylor, G. I. (1959). *The dynamics of thin sheets of fluid. II. Waves on fluid sheets.* Proc. R. Soc. Lond. A **253**, 296–312.

Taylor, G. K., Nudds, R. L., & Thomas, A. L. R. (2003). *Flying and swimming animails cruise at a strouhal number tuned for high power efficiency.* Nature **425**, 707–711.

Trapeznikov, A. A. (1957). *Application of the method of two-dimensional viscosity and shear strength to the investigation of the structure and composition of two-sided films and surface layers in solutions of soaps and saponins. Pages 242–254 of:* Proc. Second Int. Cong. on Surface Activity.

Triantafyllou, G. S. (1993). *Optimal thrust development in oscillating foils with application to fish propulsion.* J. Fluids Struct. **7**, 205–224.

Triantafyllou, M. S., Techet, A. H., & Hover, F. S. (2004). *Review of experimental work in biomimetic foils.* IEEE J. Oceanic Eng. **29**, 585–594.

Tytell, E. D., & Lauder, G. V. (2004). *The hydrodynamics of eel swimming: I. Wake structure.* J. Exp. Biol. **207**, 1825–1841.

Vandenberghe, N., Childress, S., & Zhang, J. (2006). *On unidirectional flight of a free flapping wing.* Phys. Fluids **18**, 014102.

von Kármán, T., & Burgers, J. M. (1963). *General aerodynamic theory: Perfect fluids. In: Aerodynamic Theory II*, pp. 280–310 (ed. by W. F. Durand). Dover Publications.

von Kármán, Th. (1911a). *Über den mechanismus des wiederstandes, den ein bewegter körper in einer flüssigkeit erfährt.* Nachr. Ges. Wiss. Göttingen, Math. Phys. Kl. 509–517.

von Kármán, Th. (1911b). *Über den mechanismus des wiederstandes, den ein bewegter körper in einer flüssigkeit erfährt.* Nachr. Ges. Wiss. Göttingen, Math. Phys. Kl. 547–556.

von Kármán, Th. (1957). *Aerodynamics: Selected topics in the light of their historical development.* Dover Publications.

Vorobieff, P., & Ecke, R. E. (1999a). *Cylinder wakes in flowing soap films.* Phys. Rev. E **60**, 2953–2956.

Vorobieff, P., & Ecke, R. E. (1999b). *Fluid instabilities and wakes in a soap-film tunnel.* Am. J. Phys. **67**, 394–399.

Wesfreid, J. (2006). *Scientific biography of Henri Bénard (1874–1939). In:* Dynamics of spatio-temporal cellular structures (ed. by Mutabazi, I. and Wesfreid, J. and Guyon, E.). Springer Tracts in Modern Physics. Springer Berlin/Heidelberg.

Williamson, C. H. K. (1989). *Oblique and parallel modes of vortex shedding in the wake of a circular cylinder at low Reynolds numbers.* J. Fluid Mech. **206**, 579–627.

Williamson, C. H. K. (1996). *Vortex dynamics in the cylinder wake.* Annu. Rev. Fluid Mech. **28**, 477–539.

Williamson, C. H. K., & Brown, G. L. (1998). *A series in* $1/\sqrt{\mathrm{Re}}$ *to represent the Strouhal-Reynolds number relationship of the cylinder wake.* J. Fluids Struct. **12**, 1073–1085.

Williamson, C. H. K., & Govardhan, R. (2004). *Vortex-induced vibrations.* Annu. Rev. Fluid Mech. **36**, 413–455.

Williamson, C. H. K., & Roshko, A. (1988). *Vortex formation in the wake of an oscillating cylinder.* J. Fluids Struct. **2**, 355–381.

Zdravkovich, M. M. (1969). *Smoke observations of the formation of a kármán vortex street.* J. Fluid Mech. **37**, 491–496.

Zhang, J., Childress, S., Libchaber, A., & Shelley, M. (2000). *Flexible filaments in a flowing soap film as a model for one-dimensional flags in a two-dimensional wind.* Nature **408**, 835–839.

List of symbols

Physical units are exclusively expressed in the C.G.S. system.

Roman symbols

Symbol	Unit	Interpretation
a, b, c	—	Fitting coefficients
A	cm	Lateral half-excursion of foil tip
A_0	cm	Lateral excursion of the tip of the lone flapping flag
A_D	—	Dimensionless tip-to-tip flapping amplitude
A_m	cm	Modulation amplitude
$A.R.$	—	Aspect ratio of foil, $A.R. \equiv C/D$
c_0	—	Total soap concentration in solution
c_1	—	Soap concentration in the interstitial fluid layer
c_m	—	Critical micelle concentration
C	cm	Foil chord
$C_\mathrm{L}, C'_\mathrm{L}$	—	Instantaneous lift coefficients
$C_\mathrm{D}, C'_\mathrm{D}$	—	Instantaneous drag coefficients
$\bar{C}_\mathrm{D}$	—	Mean drag coefficient
D	cm	Diameter of foil or width of flag
$\boldsymbol{e}_z$	—	Unit vector in the z-direction
E	g/(s^{2}cm)	Young's modulus
f	Hz	Foil oscillation frequency
f_0	Hz	Flapping frequency of the lone flag
f_m	Hz	Modulation frequency
f_n	Hz	Frequency of vortex wake behind a stationary object
f_p	Hz	'Preferred' frequency of flag
$F_\mathrm{D}, F'_\mathrm{D}$	dyn	Drag force on the foil

F_{D0}	dyn	Drag force on the lone flag
$F_{\mathrm{L}}, F'_{\mathrm{L}}$	dyn	Lift force of the foil
F_{P}	dyn	Propulsive force, projected onto swimming direction
G	cm	Gap width
h	μm	Soap film thickness, OR
h	—	Lateral distance between opposite-signed vortices
K	μm	Proportionality factor between c_0 and c_1
l	—	Streamwise distance between same-signed vortices
L	cm	Length scale OR length of flag (chapter 7)
L_0	cm	Length of flag
n_{i}	—	Refractive index
n	—	Integer $n = 1, 2, \ldots$
m	—	Integer $m = 1, 2, \ldots$
m_l	g/cm	Mass per unit length
M	dyn·cm	Frictional torque
p	dyn/cm^2	Pressure
P	g·m/s^3	Input power needed to sustain a flapping foil
R	g·cm^2/(K·mol·s)^2	Perfect gas constant
Re	—	Reynolds number, $\mathrm{Re} \equiv 2\pi A f D/\nu$
Re_f	—	Reynolds number, $\mathrm{Re} \equiv 2\pi R\Omega D/\nu$
Re_Ω	—	Reynolds number, $\mathrm{Re} \equiv L \cdot U/\nu$
St_{n}	—	'Natural' Strouhal number, $\mathrm{St}_{\mathrm{n}} \equiv D \cdot f_{\mathrm{n}}/U$
St_D	—	Strouhal number
St_A	—	Amplitude based Strouhal number, $\mathrm{St}_A = \mathrm{St}_D \cdot A_D$
t	s	Time
T	s	Oscillation period, $T = 1/f$
T_0, T_1	—	Constants
T_{a}	s	Advection time of leading edge layer vortices
T_{n}	s	Vortex wake period, $T_{\mathrm{n}} = 1/f_{\mathrm{n}}$
$\boldsymbol{u}$	cm/s	$\boldsymbol{u} = \boldsymbol{u}(\boldsymbol{x})$, velocity vector
U	cm/s	Free streaming flow speed
U_{tip}	cm/s	Foil tip speed
U_{eff}	cm/s	Foil tip effective speed
v_{as}	cm/s	Propagation velocity, asymmetric waves
v_{sym}	cm/s	Propagation velocity, symmetric waves

v_{M}	cm/s	Propagation velocity, symmetric Marangoni waves
$\boldsymbol{x}$	cm	$\boldsymbol{x} = (x, y)$, position vector
$\boldsymbol{x}_p$	cm	Position of vortex particle

Greek symbols

Symbol	Unit	Interpretation
α	degrees	Angle
β	degrees	Angle between $\boldsymbol{U}_{\mathrm{tip}}$ and $\boldsymbol{U}$
δ	cm	Length of a line segment
η_p	—	Propuslive efficiency $\eta_p = FU/P$
ϕ	degrees	Foil pitch angle
ϕ_{eff}	degrees	Effective angle of attack
Γ	cm^2/s	Circulation
Γ_1	—	Surface soap concentration
Γ_{01}	—	Surface soap concentration, to leading order
Γ_{m}	—	Surface soap concentration at critical micelle conc.
Γ_{le}	cm^2/s	Circulation of leading edge vortex
Γ_{te}	cm^2/s	Circulation of trailing edge vortex
κ_1, κ_2	—	Constants
λ	nm	Wave length of light
∇		Differential operator $\nabla = (\frac{\partial}{\partial x}, \frac{\partial}{\partial y}, \frac{\partial}{\partial z})$
ν	cm^2/s	Kinematic viscosity, $\nu = \mu/\rho$
ν_{b}	cm^2/s	Kinematic viscosity of bulk fluid
ν_{e}	cm^2/s	Effective kinematic viscosity of soap film
ν_{s}	cm^2/s	Kinematic viscosity of soap film surface
μ	g/(s·s)	Dynamic viscosity
ω	1/s	Scalar vorticity
Ω	1/s	Rotation rate of tower
$\boldsymbol{\omega}$	1/s	Vorticity vector
ρ	$\mathrm{g/cm}^3$	Density
σ	$\mathrm{g/s}^2$	Surface tension of soap film
σ_0	$\mathrm{g/s}^2$	Surface tension of water

σ_{m}	$\mathrm{g/s^2}$	Surface tension at the critical micelle concentration
τ	—	Dimensionless time, OR
τ	s	Time it takes a soap molecule to migrate to the surface (chapter 2)
θ	degrees	Light reflection angle

Article I

Teis Schnipper, Anders Andersen and Tomas Bohr
Vortex wakes of a flapping foil
Journal of Fluid Mechanics **633**, 411–423 (2009).

Article II

Anders Andersen, Tomas Bohr and Teis Schnipper
Separation vortices and pattern formation
Theoretical and Computational Fluid Dynamics **24**, 329–334 (2010).

Article III

Teis Schnipper, Laust Tophøj, Anders Andersen and Tomas Bohr
Japanese fan flow
Physics of Fluids **22**, 091102 (2010).

Manuscript I

Teis Schnipper and Jun Zhang

Upstream Drafting of a Flexible Body by its Downstream Neighbor

Submitted to Physical Review Letters (2010).